Evaluating cloud microphysics from NICAM against CloudSat and CALIPSO

Tempei Hashino,[1] Masaki Satoh,[1] Yuichiro Hagihara,[2] Takuji Kubota,[3] Toshihisa Matsui,[4] Tomoe Nasuno,[5] and Hajime Okamoto[2]

Received 1 August 2012; revised 6 June 2013; accepted 7 June 2013; published 8 July 2013.

[1] We describe a method to evaluate cloud microphysics simulated with a global cloud-resolving model against CloudSat and Cloud-Aerosol Lidar and Infrared Pathfinder Satellite Observation (CALIPSO) satellite data. Output from the Nonhydrostatic Icosahedral Atmospheric Model (NICAM) is run through a satellite-sensor simulator (Joint Simulator for Satellite Sensors), then directly compared to the radar and lidar signals from CloudSat and CALIPSO. The forward approach allows for consistency in cloud microphysical assumption involved in the evaluation. To investigate the dependence of the signals on the temperature, we use temperature extensively as the vertical coordinate. The global statistical analysis of the radar reflectivity shows that the simulation overestimates all the percentiles above −50°C and that snow category contributes significantly to low reflectivity values between −80 and −40°C. The simulated lidar signals have two modes associated with cloud ice and snow categories, though the observations have only one mode. The synergetic use of radar reflectivity and lidar backscatter enables us to determine the relative magnitudes of ice/liquid water contents and effective radii without use of retrievals. The radar-and-lidar diagnosis for cloud tops shows that, due to snow category, NICAM overestimates the mass-equivalent effective radius and underestimates ice water content. Also, the diagnosis was shown to be useful to investigate sensitivities of the parameters of bulk microphysical schemes on the water contents and sizes. The nonspherical scattering of ice particles was shown to affect the above radar-and-lidar diagnosis for large reflectivity ranges but not to alter most of the other diagnoses for this simulation.

Citation: Hashino, T., M. Satoh, Y. Hagihara, T. Kubota, T. Matsui, T. Nasuno, and H. Okamoto (2013), Evaluating cloud microphysics from NICAM against CloudSat and CALIPSO, *J. Geophys. Res. Atmos.*, *118*, 7273–7292, doi:10.1002/jgrd.50564.

1. Introduction

[2] To evaluate general circulation models (GCMs) and cloud-resolving models (CRMs) against satellite data, there are two main approaches: (1) comparison of a simulated aerosol/cloud variable (e.g., cloud water content) against the corresponding retrieved variable through an inversion algorithm (inversion approach), and (2) comparison of a signal (e.g., radar reflectivity and LIDAR backscatter) calculated from the output of an atmospheric model against the corresponding satellite raw observation (forward approach) [e.g., *Masunaga et al.*, 2010; *Bodas-Salcedo et al.*, 2011; *Matsui*, 2013]. The inversion approach relies on the quality of retrieval algorithm (inversion models) for model evaluation, whereas the forward approach requires forward models (or radiative transfer models) to simulate satellite-observable signals. For a given control volume, the inversion models generally have uncertainties in the physical characteristics of cloud particles, such as the phase, particle size distributions, and particle shapes. Forward models have uncertainties in radiative transfer and single-scattering properties. The inversion approach enables us to directly compare the geophysical quantities that define aerosols and clouds, such as aerosol mixing ratio and cloud and ice water contents. However, the microphysics assumptions in the cloud model may not be the same as those in the retrievals, and general users are constrained to the algorithm assumptions. On the other hand, in the forward approach the user can apply the consistent or different assumptions of microphysics properties in the forward model to investigate sensitivity of the satellite-observed signals. Because of these advantages, this study uses the forward approach for evaluating cloud properties using the satellite measurements.

[3] The forward approach has been applied to evaluate both precipitating and nonprecipitating cloud systems with

[1]Atmosphere and Ocean Research Institute, University of Tokyo, Kashiwa, Japan.
[2]Research Institute for Applied Mechanics, Kyushu University, Fukuoka, Japan.
[3]Japan Aerospace Exploration Agency, Tsukuba, Japan.
[4]NASA Goddard Space Flight Center, Greenbelt, Maryland, USA.
[5]Japan Agency for Marine-Earth Science and Technology, Yokohama, Japan.

Corresponding author: T. Hashino, Atmosphere and Oceanic Research Institute, University of Tokyo, 5-1-5, Kashiwano-ha, Kashiwa-shi, Chiba, 277-8568, Japan. (hashino@aori.u-tokyo.ac.jp)

©2013. American Geophysical Union. All Rights Reserved.
2169-897X/13/10.1002/jgrd.50564

Table 1. Definition of Symbols and Acronyms

Name	Description
BETTER	beta-temperature radar-conditioned diagram
β_{532}	532 nm lidar backscattering coefficient [1/m/str]
C1	cloud mask detected by radar
C2	cloud mask detected by lidar
C3	cloud mask detected both by radar and lidar
C4	cloud mask detected either by radar or lidar
CFED	contoured frequency by temperature diagram
CT	cloud top
IWC	ice water content
JPDF	joint probability density function
LWC	liquid water content
MPDF	marginal probability density function
PSD	particle size distribution
R_{eff}	effective radius
$R_{\mathrm{eff},m}$	mass-equivalent effective radius
T	temperature
T_b	infrared (11 μm) brightness temperature
Z_e	95 GHz radar reflectivity [dBZ]

the CloudSat and/or the Cloud-Aerosol Lidar and Infrared Pathfinder Satellite Observation (CALIPSO) satellites [e.g., *Bodas-Salcedo et al*., 2008; *Masunaga et al*., 2008; *Satoh et al*., 2010; *Shi et al*., 2010; *Zhang et al*., 2010; *Suzuki et al*., 2011; *Kodama et al*., 2012; *Zeng et al*., 2013]. In this approach, useful analyses include cloud fraction analysis and construction of marginal and joint histogram of signals such as the contoured frequency by altitude diagram (CFAD) [*Yuter and Houze*, 1995]. Also, *Zhang et al*. [2010] introduced a clustering method in order to characterize the vertical distributions of hydrometeors based on CloudSat and CALIPSO signals. *Suzuki et al*. [2011] showed that the combination of effective-radius products from the Moderate Resolution Imaging Spectroradiometer (MODIS) and CloudSat Cloud Profiling Radar (CPR) profiles are useful to evaluate simulated warm-cloud microphysical processes. In addition, precipitating clouds have been evaluated with Tropical Rainfall Measuring Mission (TRMM) Precipitation Radar (PR) and TRMM Microwave Imager [*Han et al*., 2010, *Li et al*., 2010, *Wiedner et al*., 2004], the Advanced Microwave Scanning Radiometer for Earth Observing System [*Eito and Aonashi*, 2009, *Han et al*., 2013], and Advanced Microwave Sounding Unit B and the Special Sensor Microwave Imager [*Meirold-Mautner et al*., 2007, *Shi et al*., 2010]. A systematic evaluation using the TRMM Triple-sensor Three-Step Evaluation Framework has been proposed by *Matsui et al*. [2009], where statistical analysis of signals is conducted after diagnosis of precipitating cloud types. In these previous studies, however, interpreting differences in signals relating to ice/liquid water contents, water paths, and effective radii is not straightforward.

[4] The aim of this paper is to describe an effective method to evaluate the cloud microphysical quantities as simulated by a global cloud-resolving model (GCRM). The evaluation involves using a satellite signal simulator and directly comparing the simulated signals against the satellite data set from the CloudSat CPR and the CALIPSO cloud-aerosol lidar with orthogonal polarization (CALIOP) observations [*Hagihara et al*., 2010]. The observed and simulated signals are investigated by using air temperature as the vertical axis, instead of altitude, to clearly show the dependency of cloud microphysical characteristics over the globe. In particular, the combined lidar and radar signals are used to evaluate ice/liquid water contents and effective radii qualitatively, which are essential for improving the simulated radiative heating rates and growth processes. Furthermore, we discuss the sensitivities of parameters in the bulk microphysical scheme on the effective radius and water content as well as the uncertainties in the simulated signal statistics associated with nonspherical ice scattering. The GCRM we evaluate here is the Nonhydrostatic Icosahedral Atmospheric Model (NICAM) [*Satoh et al*., 2008]. The satellite signals are simulated using the Joint Simulator for Satellite Sensors (Joint-Simulator), which is developed under the joint European Space Agency/Japan Aerospace Exploration Agency (JAXA) Earth Clouds and Radiation Explorer (EarthCARE) mission [*Gelsthorpe et al*., 2008; *Kimura et al*., 2010]. The symbols and acronyms used in this paper are listed in Table 1.

2. Data Sets

2.1. CSCA-MD, the Merged CloudSat-CALIPSO Data Set

[5] In this study, we compare simulations to the CloudSat-CALIPSO merged data set, hereafter referred to as CSCA-MD [*Hagihara et al*., 2010]. The CSCA-MD is constructed by regridding CALIOP 532 and 1064 nm attenuated backscattering coefficients into sampling volume of the CPR 95 GHz radar reflectivity (e.g., a horizontal resolution of 1.1 km, a vertical interval of 240 m, and 500 m range resolution). The altitude of the grid centers ranges from 120 to 19,800 m. In addition to the reflectivity and backscattering coefficients, the CSCA-MD contains algorithm-retrieved cloud masks, particle type, and cloud microphysical information.

[6] To identify grids containing clouds in the CSCA-MD, we use four cloud masks. The mask schemes utilize CloudSat 2B-GEOPROF (release R04) and CALIPSO lidar level 1B (version 3.01), and atmospheric profile data from the European Center for Medium-Range Weather Forecasting (ECMWF). Mask C1 uses radar data only, C2 uses lidar only, C3 uses both radar and lidar, and C4 uses either radar or lidar (Table 1). Mask C1 is based on the CPR level 2B-GEOPROF cloud mask; CPR bins with value exceeding 20 are labeled cloud. Because the lowest 1 km bins of the CPR observations contain surface-clutter signals, we exclude them from the analysis. Mask C2 uses a threshold of the 532 nm attenuated total backscattering coefficient and a spatial continuity test. C2 differs from the vertical feature mask [*Vaughan et al*., 2005], the original CALIPSO lidar level 2 mask, having less contamination by noise and aerosols at low altitude levels [*Hagihara et al*., 2010; *Okamoto et al*., 2010; *Rossow and Zhang*, 2010]. C1 and C2 are interpolated onto the unified grid. Mask C3 labels a grid box as cloud if both of the averaged C1 and C2 exceed 0.5, whereas C4 requires only one of the averaged (C1 or C2) masks to exceed 0.5.

2.2. NICAM Joint-Simulator Simulated Merged Data Set

[7] We use a high-resolution global data set produced by NICAM, a global cloud-resolving type numerical model (GCRM). For forward simulations, a GCRM has advantages over traditional coarse-resolution GCMs: (1) a GCRM does not require the additional schemes for generating subgrid

Table 2. Hydrometeor Categories and Parameters Used in Forward Calculation With NICAM Single-Moment Water 6 (NSW6)[a]

	Particle Size Distribution	Specified Parameters	Fixed Density or *m-D* Relation
Cloud water	*Mono-disperse: $N = N_T\ \delta(R\text{-}R_{\mathrm{eff}})$ [1/cm^3]	*$R_{\mathrm{eff}} = 8$ [μm]	1 [g/cm^3]
Rain	Inverse exponential: $N(D) = N_0 \exp(-\lambda D)$ [1/cm^4]	$N_0 = 0.08$ [1/cm^4]	1 [g/cm^3]
Cloud ice	*Mono-disperse	*$R_{\mathrm{eff}} = 40$ [μm]	*$a = 0.1677$, $b = 2.91$ [CGS]
Snow	Inverse exponential	$N_0 = 0.03$ [1/cm^4]	0.1 [g/cm^3]
Graupel	Inverse exponential	$N_0 = 0.04$ [1/cm^4]	0.4 [g/cm^3]

[a]The items with asterisk are not defined in NSW6 for microphysical calculation. R and D are the radius and diameter of hydrometeors. N_T is the total number concentration for the mono-disperse distribution. The mass-dimensional (*m-D*) relation is given as $m = a\ D^b$.

cloud variability [e.g., *Klein and Jakob*, 1999], and (2) microphysical assumptions necessary for the forward calculation can be mostly consistent to the GCRM's microphysics formulation. That is, with a GCRM, simulated signals can be easily linked to the relevant assumptions in the cloud microphysical scheme.

[8] The NICAM experiment in this study was originally designed to study the tropical cyclone (TC) Fengshen from the genesis stage to the mature stage (T. Nasuno et al., Genesis of typhoon Fengshen (2008) from vortex superposition. Part I: Large-scale conditions, submitted to *Journal of the Atmospheric Sciences*, 2013). The winds, temperature, relative humidity, and geopotentials in the NICAM simulation were initialized with the 0.5° × 0.5° ECMWF Year of Tropical Convection analysis [*Waliser et al*., 2012] at 00:00Z 15 June 2008. The surface variables such as sea surface temperature (SST), sea ice cover, and soil moisture are initialized with the 1° × 1° National Centers for Environmental Prediction reanalysis. The SST was nudged to the National Oceanic and Atmospheric Administration weekly optimum interpolation SST analysis [*Reynolds and Smith*, 1994] with a 5 day relaxation time, whereas the others are integrated without nudging. The average horizontal grid spacing is 3.5 km, while the vertical grid has 40 levels of grid size, ranging from 162 m at the surface to 3012 m at the top of the atmosphere [see *Satoh et al*., 2010, Table 1].

[9] The cloud microphysics scheme is a single-moment bulk microphysical parameterization, called the NICAM Single-moment Water 6 (NSW6) [*Tomita*, 2008]. NSW6 predicts mass mixing ratios of six water categories: water vapor, cloud water, rain, cloud ice, snow, and graupel. It is based on *Lin et al*. [1983] and *Rutledge and Hobbs* [1983] but omits the wet growth of hail in order to reduce computation cost. The main difference is that cloud water and cloud ice are generated only by a saturation-adjustment scheme.

[10] In the forward simulation, we transform the NICAM's output (geophysical parameters) to simulated satellite signals using the Joint Simulator for Satellite Sensors (https://sites.google.com/site/jointsimulator/), a multisensor, multi-instrument satellite simulator. The Joint-Simulator was created in support of the EarthCARE mission and weather and climate models. It is capable of simulating EarthCARE's four sensors (a cloud/aerosol lidar, a cloud profiling radar with Doppler velocity measurement, a multispectral imager, and a multiview broadband radiometer). However, the Joint-Simulator is flexible enough that it can be applied to the simulation of CloudSat and CALIPSO signals in addition to existing satellite sensors, including TRMM sensors. The basic structure of the Joint-Simulator is inherited from the Satellite Data Simulator Unit (SDSU) [*Masunaga et al*., 2010]. The software infrastructure is developed upon the NASA-Open-Released G-SDSU Version 2 Core Modules (http://opensource.gsfc.nasa.gov/projects/G-SDSU/), which features flexible module interface and message-passing interface modules. Thus, the Joint-Simulator enables fast computation of signals with the large size of model input in a cluster computer. The specific simulators we used were as follows: the EarthCARE Active Sensor simulator (EASE) for radar and lidar [*Okamoto et al*., 2003, 2007, 2008; *Nishizawa et al*., 2008], RSTAR6b for visible and infrared radiometers [*Nakajima and Tanaka*, 1986, 1988; M. Sekiguchi, personal communication, 2009], and MSTRN X for broadband radiometers [*Sekiguchi and Nakajima*, 2008]. All the simulators calculate level 1 raw signals or level 2 products from a vertical column of the atmosphere with the assumption of a plane-parallel atmosphere.

[11] EASE, the primary forward simulator here, calculates Z_e, the attenuated radar reflectivity at 95 GHz (in units dBZ), and β_{532}, the attenuated backscattering coefficient at 532 nm (in units 1/m/ster) based on the NICAM-simulated atmospheric profiles. The simulator accounts for the attenuation by hydrometeors in radar and lidar signals and the molecular attenuation and backscattering in lidar signals. We also use *Ishimoto and Masuda's* [2002] multiple-scattering table to account for multiple scattering by liquid hydrometeors in the lidar signals.

[12] The forward simulation requires the parameterization of particle size distributions (PSDs) and mass-dimensional relationships for hydrometeor categories, since NSW6 neither prognoses or diagnoses these parameters. The information used for NSW6 is listed in Table 2. Those for rain, snow, and graupel categories are taken from NSW6. However, the PSDs are not defined for cloud water and cloud ice categories in NSW6. To be consistent with calculation of radiative heating rates in NICAM, the mono-disperse size distributions with effective radii R_{eff} of 16 μm and 40 μm were specified for cloud water and cloud ice categories, respectively. In addition, a mass-dimensional relationship (i.e., effective density) is not defined for cloud ice category in NSW6. Thus, it was assumed to be one corresponding to the cold hexagonal columns of *Mitchell* [1996].

[13] For the EASE-simulated CPR and CALIOP signals, the C1, C2, C3, and C4 masks were made to be similar to those of the observations. C1 for the simulation simply defines a cloudy box with the radar reflectivity threshold of −30 dBZ. C2 uses the threshold of the backscattering coefficient defined in equation (1) of *Hagihara et al*. [2010] (minus the noise terms):

$$\beta_{th}(z) = \frac{\beta_{th,\mathrm{aerosol}} + \beta_m(z)}{2} - \frac{\beta_{th,\mathrm{aerosol}} - \beta_m(z)}{2} \tanh(z-5), \quad (1)$$

where z is the altitude (km), $\beta_{th,\mathrm{aerosol}} = 10^{-5.25}$ (1/m/ster), and $\beta_m(z)$ is the volume molecular backscattering coefficient calculated from the NICAM output. The spatial tests of *Hagihara et al*. [2010] were not required, because of no instrumental noise in our forward model. As is done for the observations, the simulated radar signals within 1 km of the surface are excluded, mimicking the surface-clutter effect in the observations. Similarly, since CloudSAT and CALIPSO observations are limited to ±82° latitude, simulated signals are also limited to the same latitudinal range. The vertical sampling of EASE is identical to that of the CSCA-MD, but the horizontal footprint remains the same as the horizontal grid spacing (3.5 km) of the NICAM simulation, which differs from that of the CSCA-MD. Since CloudSat CPR is 1.1 km footprint size, we assume this difference does not significantly affect our conclusions.

[14] The time period of the global simulation data set is from 00:00Z 17 June to 00:00Z 25 June 2008. Seven days of CloudSat and CALIPSO observations do not contain enough spatial samples for a statistically significant comparison (the observations are columns of profiles). Thus, we sampled observation data from the entire month of June to make robust statistical data sets. Since 1 month of the global simulation is not feasible due to the computational expense at this moment, we assume that the cloud population, microphysics, and global cloud statistics for 7 days are similar to those for the entire month. We conducted the cloud fraction analysis and in-cloud analysis for the first and second 2 weeks of the month. These show that the two signal statistics are very similar, although the spatial distributions of cloud fraction show some differences. To save computation time in the statistical analysis, simulation samples were taken every four grid points and every 12 h.

2.3. Determining the Particle Phase

[15] In order to determine the hydrometeor phase (liquid or ice) in the observation, the lidar retrieval product in the CSCA-MD was used. The mass ratio of the model hydrometeors was used for the simulations. *Yoshida et al*. [2010] developed a method to discriminate the particle type using the depolarization ratio (δ) and the ratio of the attenuated backscattering coefficients for two vertically consecutive layers (x). Three-dimensional ice and 2-D plate types were used for ice while warm and supercooled water types for liquid. Large δ and x are basically associated with cloud layers of spherical liquid water due to the large effects of multiple scattering and attenuation. Due to the difficulty in simulating the depolarization ratio associated with multiple scattering and different particle shapes, we use the mixing ratios of the hydrometeor categories for simulation. If the ratio for liquid exceeds 80% in a given box, the entire box is labeled as liquid. The same holds for the ratio for ice. The ratio, 80%, is subjectively determined to ensure the dominant signals from liquid hydrometeors, but uncertainty remains on the correspondence to the particle type retrieval.

2.4. Multiple-Scattering Detection

[16] CloudSat CPR observations of deep tropical convective cores can be also contaminated by multiple scattering (MS). For example, above the freezing level height, more than 35% of the range bins can be contaminated [*Battaglia et al*., 2011]. Since it is not easy to extract the information from the contaminated grids, we simply remove the simulated and observed signals from statistical analysis below a height where MS becomes significant. In order to identify the height, the altitude of MS onset H_{MS} is used, which was derived by *Battaglia et al*. [2011] for deep convective profiles. To determine H_{MS}, the following vertically integrated variable is calculated:

$$I(z)_{>\widetilde{Z}} = 10\log_{10}\left[\int_z^{\mathrm{TOA}} \max\left\{Z_{\mathrm{obs}} - \widetilde{Z}, 0\right\}(z)\mathrm{d}z\right], \quad (2)$$

where Z_{obs} is the attenuated radar reflectivity and $\widetilde{Z}$ is a threshold of 8 dBZ. H_{MS} is the level z where $I(z)_{>\widetilde{Z}}$ reaches 41.9 dBZ.

[17] *Battaglia et al*. [2011] defines the deep convective profiles with two criteria: (1) deep convection identified with the 2B-CLDCLASS product and (2) profiles with reflectivity exceeding 0 dBZ above 10 km. Since the 2B-CLDCLASS product is not applicable for the NICAM simulation, we apply criteria to remove stratiform profiles. Vertical profiles of the 95 GHz Z_e in stratiform precipitation are known to exhibit a local minimum just below the 0°C isotherm. It is called the dark band, one of the features used to identify stratiform precipitation [*Kollias and Albrecht*, 2005]. We identify the dark band if the maximum Z_e above the freezing level is more than 5 dBZ and the Z_e just below the freezing level is less than the maximum Z_e below the freezing level. Thus, in this study, deep convective profiles are defined upon the columns that satisfy the above criteria (2) without the dark band.

2.5. Nonspherical Ice Scattering

[18] The single-scattering library in EASE consists of ice sphere model calculated with Mie theory and six nonspherical ice models calculated with the discrete dipole approximation [*Sato and Okamoto*, 2006; *Okamoto et al*., 2010]. The nonspherical models include five single-habit and one mixed-habit nonspherical ice models: bullet-rosettes, hexagonal columns, and hexagonal plates oriented randomly in three dimensional plane (3-D bullet-rosette, 3-D column, and 3-D plate), hexagonal columns and hexagonal plates oriented in horizontal plane (2-D column and 2-D plate), and mixture of 50% of 2-D column and 50% of 3-D bullet-rosette model (CB50).

[19] In general, there are uncertainties in the simulated signals due to ambiguity in the model representation of cloud microphysics. The simulated signals are very sensitive to assumed shape (or habit) and orientation of ice particles especially for high-frequency microwave measurements such as CloudSat 95 GHz CPR [e.g., *Sato and Okamoto*, 2006; *Liu*, 2008; *Kulie et al*., 2010]. As pointed out above, cloud ice in NSW6 does not have information on the habit and orientation, leading to some uncertainty in the signals related to cloud ice. It has been shown that the spread in simulated Z_e increases with $R_{\mathrm{eff},m}$ under a fixed ice water content (IWC), reaching 7–8 dB (~3 dB) for $R_{\mathrm{eff},m}$ larger (smaller) than 200 μm [*Okamoto*, 2002; *Sato and Okamoto*, 2006; *Okamoto et al*., 2010]. Similarly, the spread in simulated β_{532} increases with $R_{\mathrm{eff},m}$ and gets up to more than a half order for $R_{\mathrm{eff},m}$ larger than 100 μm [*Okamoto et al*., 2010].

[20] In addition, unavoidable mismatches of assumptions between microphysics schemes and forward simulators may exist to some extent. EASE stores the single-scattering lookup tables as a function of mass-equivalent effective radius $R_{\mathrm{eff},m}$. In the current version of EASE, the single-scattering properties of ice categories in a grid box are calculated using only one of the predefined ice models. However, in NSW6, snow and graupel are both spherical particles but with different densities (Table 2). Therefore, there is a limitation in matching up the habits in NSW6 with those in the single-scattering library.

[21] In section 3, we compare the signals calculated with ice sphere against the observation first. Then, the potential impacts of nonspherical scattering on the diagnosis are discussed.

3. Results

3.1. Example Profiles

[22] By directly comparing the vertical profiles for a certain cloud type, we can better understand the statistical analysis and the spatial characteristics of the simulated signals. In the following, we consider the observed and simulated signals for tropical cyclone (TC) Fengshen and a midlatitude synoptic disturbance. These were chosen because the TC development was the target of the simulation, and these systems have a large spatial scale and long lifetime that can be easily observed by nadir-looking polar-orbit satellites.

[23] Figure 1a shows the observed infrared (11 μm) brightness temperature (T_b) at 17:30Z 19 June for TC Fengshen. At this time, convective activity appears to be more active south of the TC center (white cross) than north. The NICAM simulation at 12:00Z 19 June captures the observed asymmetric convective activity well (Figure 1b). However, the simulation shows more isolated convective cells with less spread of detrainment than the observation.

[24] The color fill in Figure 1c shows the observed 95 GHz radar reflectivity (Z_e) with the C1 mask at 17:20Z. Z_e at 7°N–9°N have a local minimum just below the 0°C isotherm (green line) in the vertical profiles, i.e., the dark band. Z_e above 8 km, hereafter the upper levels, is largest at 9°N–10°N, and this region also has high 532 nm backscattering coefficient (β_{532}) at the cloud top (Figure 1e). The white lines are the H_{MS} level proposed by *Battaglia et al.* [2011] for deep convective profiles. Therefore, Z_e at altitudes below 8–10 km in the region may be heavily affected by MS. These observations suggest that the profiles at 9°N–10°N are characterized with convective cells. Regarding the corresponding simulation, a Z_e cross section was taken to pass through the TC center (Figure 1d). The Z_e values at the upper level at 6.1°N–6.4°N and 11.4°N–11.8°N are higher than the surroundings, indicating convective activities. Moreover, the H_{MS} values over 10.8°N–11°N and 11°N–11.2°N suggests strong convection in the profiles. This large Z_e and H_{MS} signals are indeed accompanied by strong vertical motion in dynamics (not shown). Above 4 km, the graupel mass content is large, exceeding 1 gm^{-3} in places, with similar rain mass contents below 4.5 km. This leads to strong attenuation of the signals below the H_{MS}, causing the absence of signals in the convective columns that appear to be an arch shape. The lack of signals is most likely due to the lack of a MS parameterization in EASE. Surprisingly, there are profiles with the dark band at 6.5°N–7°N and 10°N–10.8°N, similar to the observed profiles at 8°N–9°N, even though the cloud microphysical scheme is a single-moment scheme and ice scattering models for melting ice particles were not used. Comparison of Figures 1c and 1d indicate that the simulation tends to overestimate the Z_e at the upper level in and around the active convection, implying overproduction of large ice particles.

[25] According to Figures 1e and 1f, both the observation and simulation show relatively large β_{532} at the top of the convective profiles compared to the surroundings. This implies that the simulation captures the microphysical characteristics of the convective profiles also in β_{532}, i.e., a change in ice water content and/or effective radius.

[26] The area enclosed by the black contours in Figures 1c–1f is the region of the C3 mask. In the observation, the depth of the C3-mask region varies from about 2 to 4 km but is relatively small over the convective regions due to the larger water content there. Outside of the convective regions, the C3-mask area has Z_e less than about −5 dBZ. These features are well simulated except that the depth of the simulated C3 is occasionally quite deep and Z_e tends to be overestimated away from the convective regions. This suggests that the upper clouds underestimate the optical thickness due to less IWC and/or larger R_{eff} than the observation, which is consistent with "more isolated" cells seen in the IR images.

[27] Figure 2a shows the observed T_b for a frontal cloud system in the Southern Hemisphere at 19:30Z 19 June, which was observed by CloudSat and CALIPSO at 19:14Z (Figures 2c and 2e). Due to the dark band under the sloping 0°C isotherm (Figure 2c), most of the profiles at 38°S–41°S appear to be stratiform. The observed β_{532} with C2 (Figure 2e) is large at the altitude of 7 km over 41°S, suggesting the top of a convective cloud, possibly triggered by the frontal lifting. Interestingly, β_{532} values tend to be larger than those of the TC case. The simulated counterparts at 12:00Z 19 June are shown in Figures 2b, 2d, and 2f for a frontal system near the observation. The simulation tends to overestimate and give a corrugated texture to T_b, while the location of the system is well captured. The simulated cloud top identified from β_{532} with the C2 mask is similar to observations, but the values are smaller. This suggests that the simulated cloud tops are optically thinner, causing the warmer T_b and deeper region of C3. In addition, the simulation tends to underestimate the occurrences of large Z_e (>10 dBZ) for the frontal case.

[28] Horizontally averaged signals were calculated with the ice sphere and the six nonspherical ice models for the midlatitude profiles shown in Figure 2. The differences between the mean signals with the nonspherical model and those with the sphere (or mean of Z_e (nonspherical model) − Z_e (Mie)) are shown in Figure 3a. The spread of the mean differences increases downward as the mean Z_e (Mie) increases. The mean Z_e by 3-D models is mostly less than that by the sphere model. On the other hand, the 2-D models and combined model (CB50) produce larger mean Z_e throughout the layers. Use of 2-D plate leads to about 5~7 dB larger than the sphere model below 6 km, and the Z_e is in the close range of the observed Z_e. Three-dimensional plate, however, produces as much as −2.5 dB below 6 km. This highlights the importance of orientation of the ice

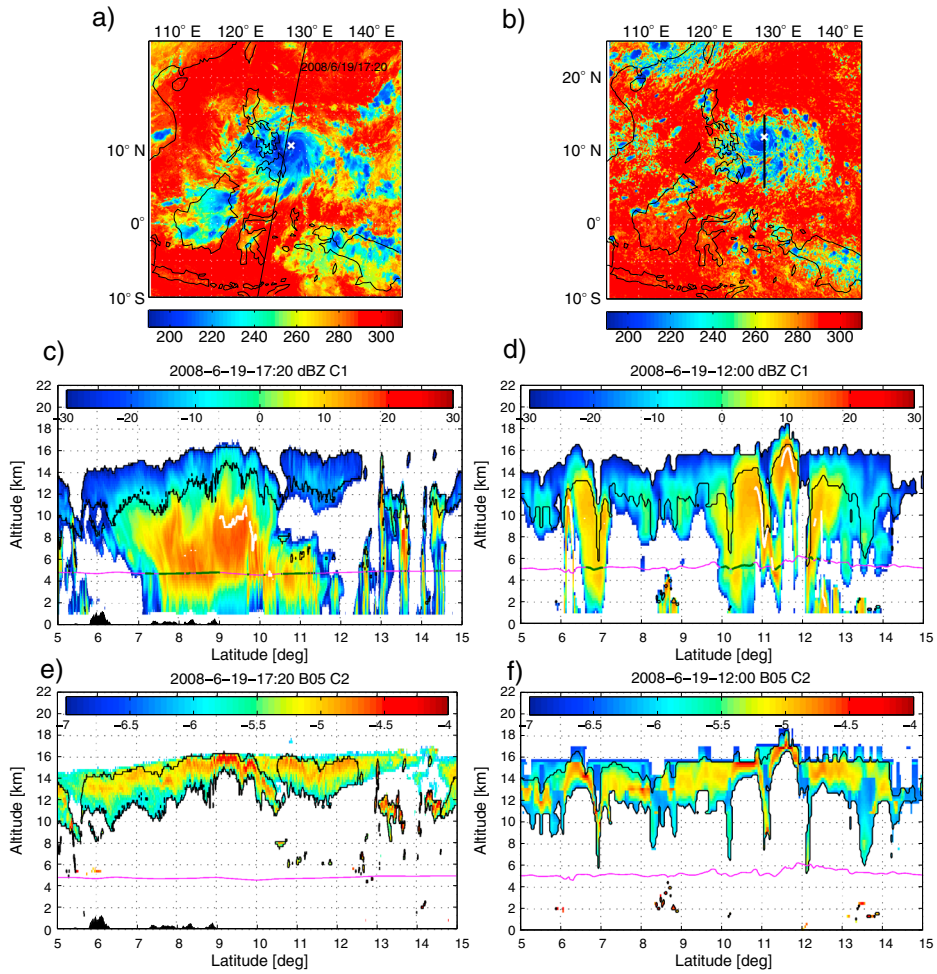

Figure 1. Observed and simulated remote-sensing data. (a) Observed and (b) simulated infrared (10.8 μm) T_b from MTSAT. (c) Observed and (d) simulated 95 GHz radar reflectivity from CloudSat with the C1 mask. (e) Observed and (f) simulated 532 nm backscattering coefficient from CALIPSO with the C2 mask for Tropical Cyclone Fensheng. The orbit of CloudSat and CALIPSO is shown as the black line in Figure 1a. The observation time for MTSAT is 19 June, 17:30Z 2008, while that for CloudSat and CALIPSO is 19 June, 17:20Z. The simulation time is on 19 June, 12:00Z 2008. The black line in Figure 1b marks the cross-section location. The TC center is indicated by a white cross. The observed center is taken from Japan Meteorological Agency best track data at 18:00Z. The black contours in Figures 1c, 1d, 1e, and 1f indicate the region of C3. The white lines in Figures 1c and 1d indicate the altitude of multiple-scattering onset as proposed by *Battaglia et al*. [2011]. The magenta lines mark the 0°C isotherm, and some of the isotherm is colored with green if the dark band exists below.

particle as well as the habit. As for the β_{532} (Figure 3b), use of the nonspherical models results in the larger signals within 3 km from the C2 cloud tops than the ice sphere as much as 0.28 in units log10 of 1/m/str. Then, the smaller signals are simulated with the nonspherical models close to the C2-defined cloud base due to larger attenuation of the signals above. Again, the use of 2-D plate can increase the β_{532} up to the observed one. After all, the ranges of the spread in the simulated Z_e and β_{532} are consistent with the previous researches mentioned in section 2.5. Using 2-D plate compensates underestimation of IWC with the strong backscattering. According to the retrieved cloud particle types by *Yoshida et al*. [2010], 2-D plate mainly occurs for between −20 and −10°C of more than 10% of clouds, and 3-D ice type tends to occur below −20°C. In addition, the pointing angle of CALIPSO is about 3° off-nadir at this time period of observation, suggesting that high β_{532} in the observation may not stem from the specular reflection by 2-D plate. Therefore, we speculate that even if we use a realistic combination of ice models based on habit occurrences, the simulated Z_e and β_{532} would be underestimated for the midlatitude profiles.

3.2. Global Contoured Frequency by Temperature Diagram (CFED)

[29] To better understand the in-cloud statistics, we bin the global samples of radar and lidar observations by temperature (T) and signal value. Then, for each T range, we normalize the joint probability density function (JPDF) and call the resulting diagram CFED for contoured frequency by temperature diagram (following CFAD in *Yuter and Houze*, 1995). This way, signal characteristics at each T (or altitude) can be

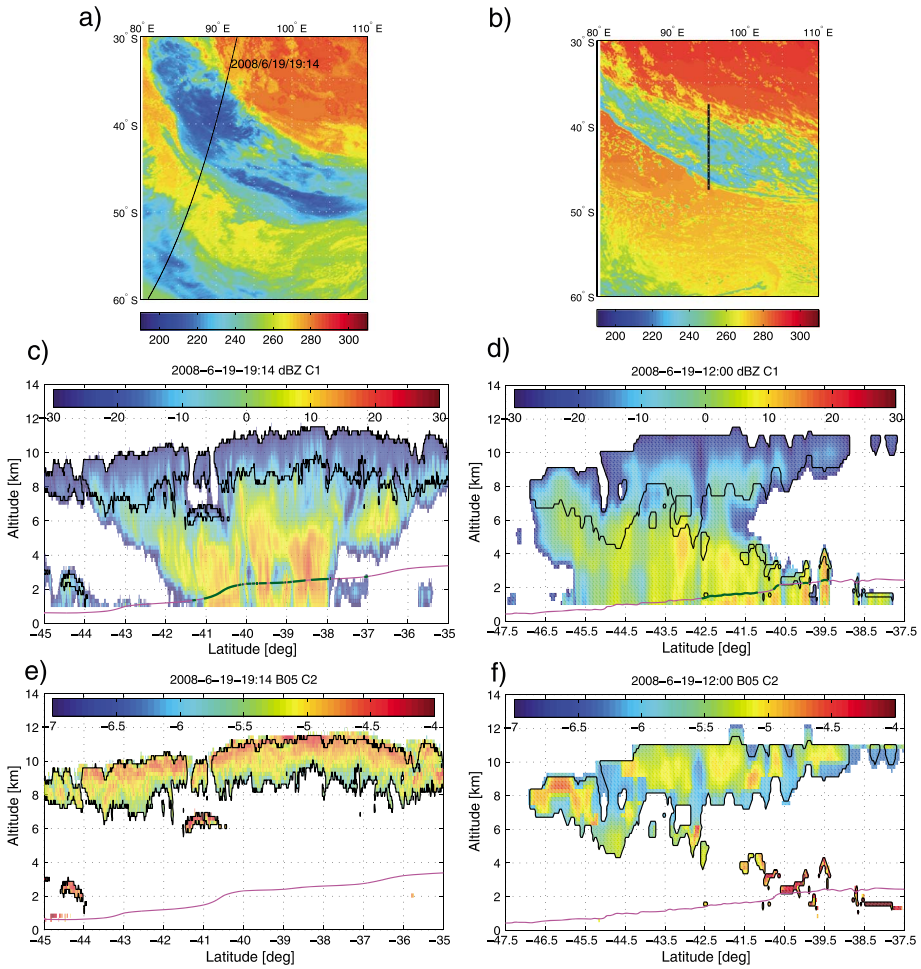

Figure 2. Same as Figure 1 except for a midlatitude system. The observation times are 19 June, 19:30Z 2008 for MTSAT and 19 June, 19:14Z for CloudSat and CALIPSO. The simulation time is 19 June, 12:00Z 2008.

easily associated with cloud microphysical processes. As a temperature-altitude reference, we show in Figure 4 the zonal monthly mean and standard deviation of T, with the ECMWF analysis on the left and the NICAM simulation on the right. Their similarity in the mean suggests that clouds in a range of T from the CSCA-MD and the NICAM simulation are located in a similar altitude range. The 5 K change roughly corresponds to a vertical distance of about 1 km at low levels over the tropics and about 0.67 km for other regions of the troposphere.

[30] When plotted against Z_e and T, the observed and simulated CFEDs have a dominant mode at T less than 0°C (Figures 5a and 5b). For a regional scale, the freezing level does not vary much; thus, the signals plotted against the altitude show a similar dominant mode. However, the climatological freezing level varies over latitudes for the global samples. Such regional characteristics of Z_e signals are smeared out, and the mode cannot be seen if the altitude is used as the vertical coordinate. For example, the slope and intercept parameters of the Marshall-Palmer distribution depend on temperature for aggregation-dominant clouds [e.g., *Houze et al.*, 1979; *Heymsfield et al.*, 2002]. Such a dependency of cloud microphysical parameters and the resulting signals on temperature can be easily seen by using temperature as the vertical axis.

[31] Above the freezing level, the NICAM simulation concentrates the signals around a mode. This could imply a lack of degree of freedom in the ice water content and effective radius simulated with the single-moment bulk scheme, as also pointed out for Met Office global forecast model [*Bodas-Salcedo et al.*, 2008]. Since none of the other ice scattering models result in a broad distribution like the observation (as discussed below), the above-mentioned limitation of the single-moment bulk scheme is probable. At T below −20°C, the simulated mode appears to be shifted upward compared to the observation, and above −50°C all the percentiles are overestimated. Below the freezing level, the observed CFED has one mode associated with the nonprecipitating regime and one mode from attenuation by raindrops that were possibly produced by melting of ice particles. Similarly, the simulated CFED indicates a large contribution from the precipitating regime. The simulation overestimates the occurrence between −10 and 10 dBZ as indicated by the marginal probability density function (MPDF) over Z_e.

[32] The global CFEDs of $\log10(\beta_{532})$ for the CSCA-MD and the NICAM simulation with the C2 mask are shown in

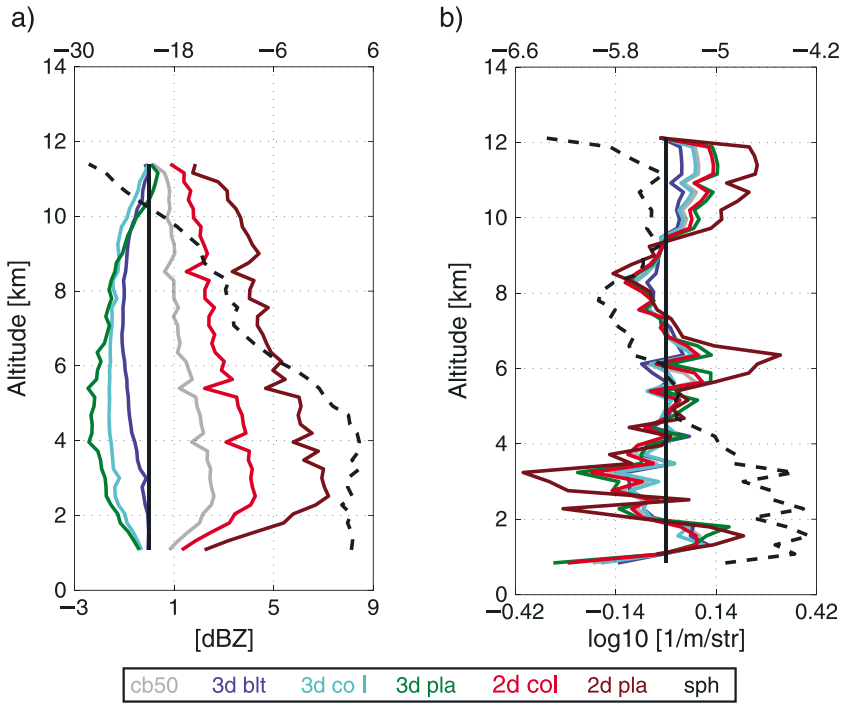

Figure 3. Differences between the horizontally averaged signals calculated with the six nonspherical ice models and those with the ice sphere model for the midlatitude profiles shown in Figure 2. (a) 95 GHz radar reflectivity, (b) 532 nm lidar backscattering. The horizontal mean of the signals with the ice sphere model is also shown with broken lines.

Figures 5c and 5d. The MPDF of the observed log10(β_{532}) has peaks at −5.2 and −3.8 in units log10 of 1/m/str, whereas that from simulations has an additional peak at −6.2. The observed CFED shows two modes, one mode at T below −20°C and another at T near −5°C and log10(β_{532}) around −4. The lower mode stems from supercooled and warm liquid clouds as seen in Figure 6 of *Yoshida et al.* [2010]. Similarly, the CFED for the simulation has a mode associated with liquid hydrometeors at T above −5°C and log10(β_{532}) near −4. For the liquid clouds, the simulation underestimates the 75th and 95th percentiles. The simulated high ice clouds have two modes, one near −6.2 and another at −5.2 above the −40°C level. As a result, the simulation underestimates the 5th and 25th percentiles at T below −5°C.

[33] Although the sensitivity of the simulated signals to ice scattering models can be large relative to the spread due to IWC and sizes, the differences in the percentiles between the observed and simulated signals remain qualitatively similar among the ice models for the simulated IWC and particle sizes. To investigate the impacts on global statistics, the global CFEDs of Z_e and β_{532} were constructed with use of the nonspherical models. Figures 6a and 6b compare the 25th, 50th, and 75th percentiles of Z_e and the interquartile range (IQR) calculated with the seven ice models. For these percentiles, 2-D plate and 2-D column simulate larger Z_e than the ice sphere model, while 3-D bullet, 3-D column, and 3-D plate show smaller Z_e than the sphere model. The spread of the 50th (75th) percentiles among the ice models increases

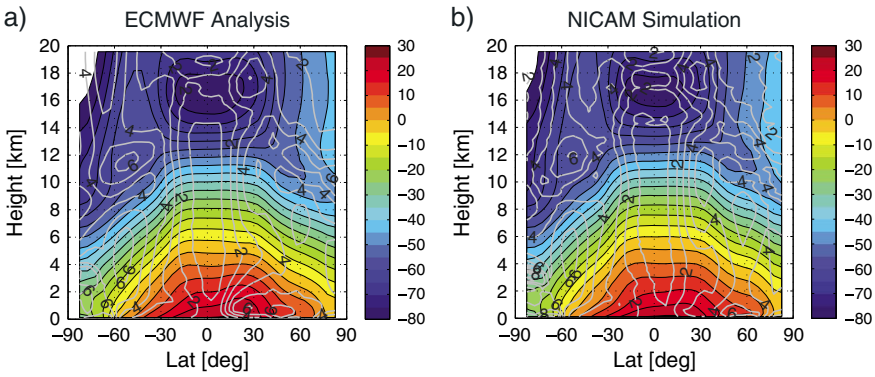

Figure 4. Zonal mean (color fill) and standard deviation (contour) of air temperature. (a) Calculated with ECMWF analysis over the month of June 2008. (b) Modeled with NICAM for 00:00Z 17 June 2008 to 00:00Z 25 June 2008.

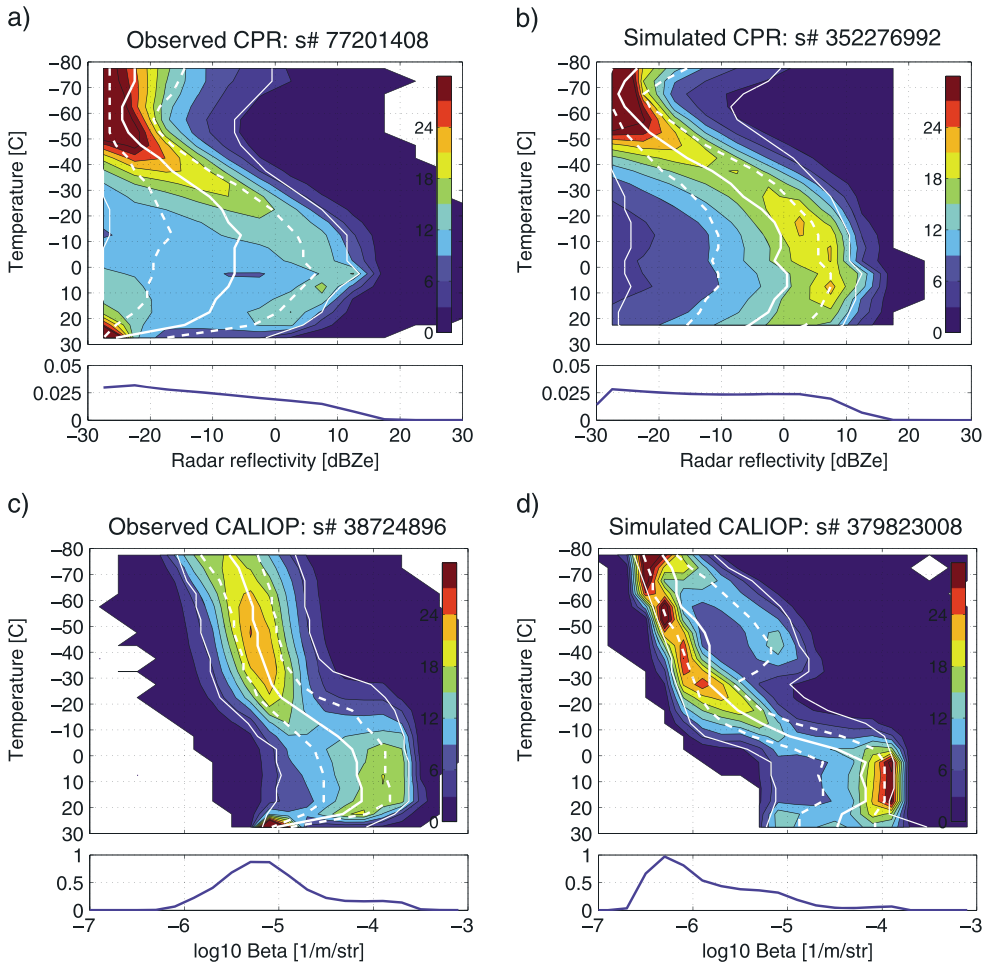

Figure 5. Global CFED for 95 GHz radar reflectivity with C1 and 532 nm lidar backscattering with C2. (a) From CSCA-MD for 95 GHz radar reflectivity. (b) From the NICAM simulation for 95 GHz radar reflectivity. (c) From CSCA-MD for the 532 nm lidar backscattering. (d) From the NICAM simulation for the 532 nm lidar backscattering. The colorfill shows 100 times the JPDF-normalized value at each temperature. The bin widths for the temperature, radar and lidar signals are 5 K, 5 dBZ, and 0.2 log10[1/m/str], respectively. The white thick solid curves are the median, the white broken lines are the 25th and 75th percentiles, and the thin white solid curves are the 5th and 95th percentiles. The MPDFs in terms of the signals are shown in the bottom panels. The total number of samples is shown with "s#" in the titles.

with T, reaching a maximum of ~7 (8) dB at $-20 < T < 0$°C (at $-30 < T < 0$°C). Note that the 50th percentiles simulated with 2-D plate are as large as the 75th calculated with the 3-D models. On the other hand, variation of the IQR of Z_e among the ice models is up to 4 dB. The spread of the Z_e simulated with the different scattering models at a T range can be as large as about a half of the spread that stems from the IWC and particle size. As for β_{532}, the spread due to the ice models is also as large as a half of the IQR at $T < -15$°C (Figures 6c and 6d). Again, 2-D plate model results in the largest percentiles at $T < -15$°C. Considering the effects of the particle shapes and orientations, the following conclusion is derived: the Z_e percentiles are overestimated by the simulation at $T > -50$°C, and the β_{532} percentiles are underestimated over all the T range.

3.3. Separation of Contribution by Hydrometeors to Signals

[34] To improve the radar and lidar signals from the simulation, one must identify the space dominated by each hydrometeor category in the CFED. The contribution of a category h in the bin of signal x_i and temperature T_k are calculated as

$$C^h(i,k) = 1 - \frac{N^{T-h}(i,k)}{N^T(i,k)}, \tag{3}$$

where $N^{T-h}(i,k)$ is the number of samples in the bin calculated with EASE by switching off the mass mixing ratio of category h, and $N^T(i,k)$ is the number of samples in the bin with all the categories. The difference between the signals with all categories and those with a subset of categories arises from the contributions of both extinction and backscattering cross sections from the excluded category. If $C^h(i,k) = 1$, then all of the signals in (i,k) are explained (or produced) with inclusion of category h. If the number of signals in the bin increases without the category, $C^h(i,k)$ can be negative.

[35] The contribution of a hydrometeor category is easily identified with the $C^h(i,k)$ and almost mutually exclusive. Figure 7 shows $C^h(i,k)$ of hydrometeor categories for the

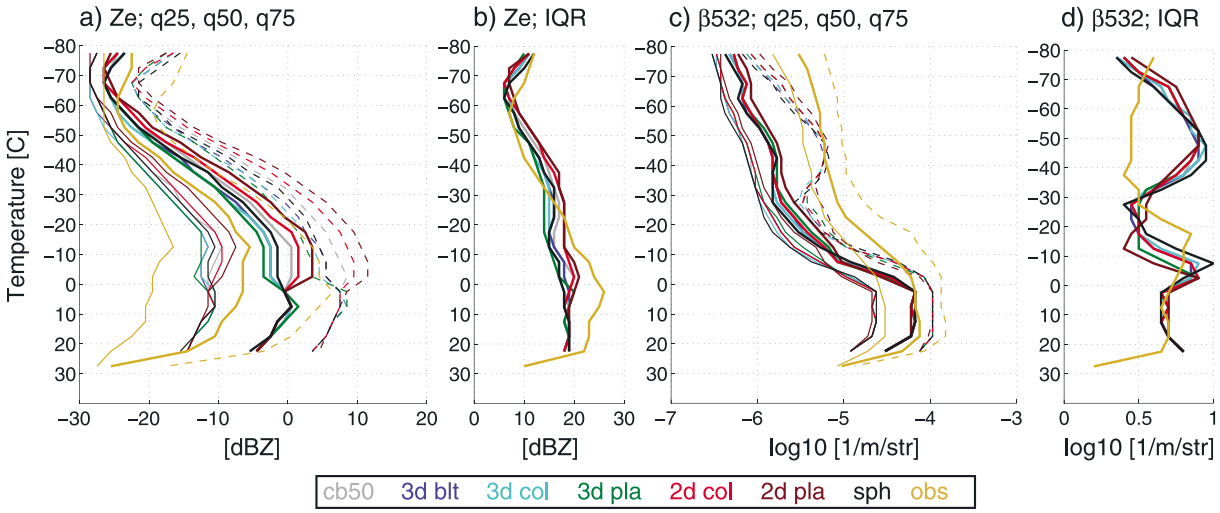

Figure 6. Comparison of percentiles calculated with nonspherical ice scattering tables for the global C1 and C2 CFEDs. The 25th, 50th, and 75th percentiles (q25, q50, and q75) for (a) radar reflectivity and (c) lidar backscattering coefficient. (b and d) The IQR = q75–q25.

global CFED of the Z_e. The dominant mode between −80 and −40°C and at Z_e smaller than −20 dBZ seen in Figure 5b is produced by snow and cloud ice categories, with the smaller Z_e and T between −80 and −65°C contributed by cloud ice (Figure 7a), but somewhat surprisingly, snow category contributes most to the mode (Figure 7b). The mode between −40 and −20°C is mostly explained by snow category, and the mode between −20 and 0°C is explained

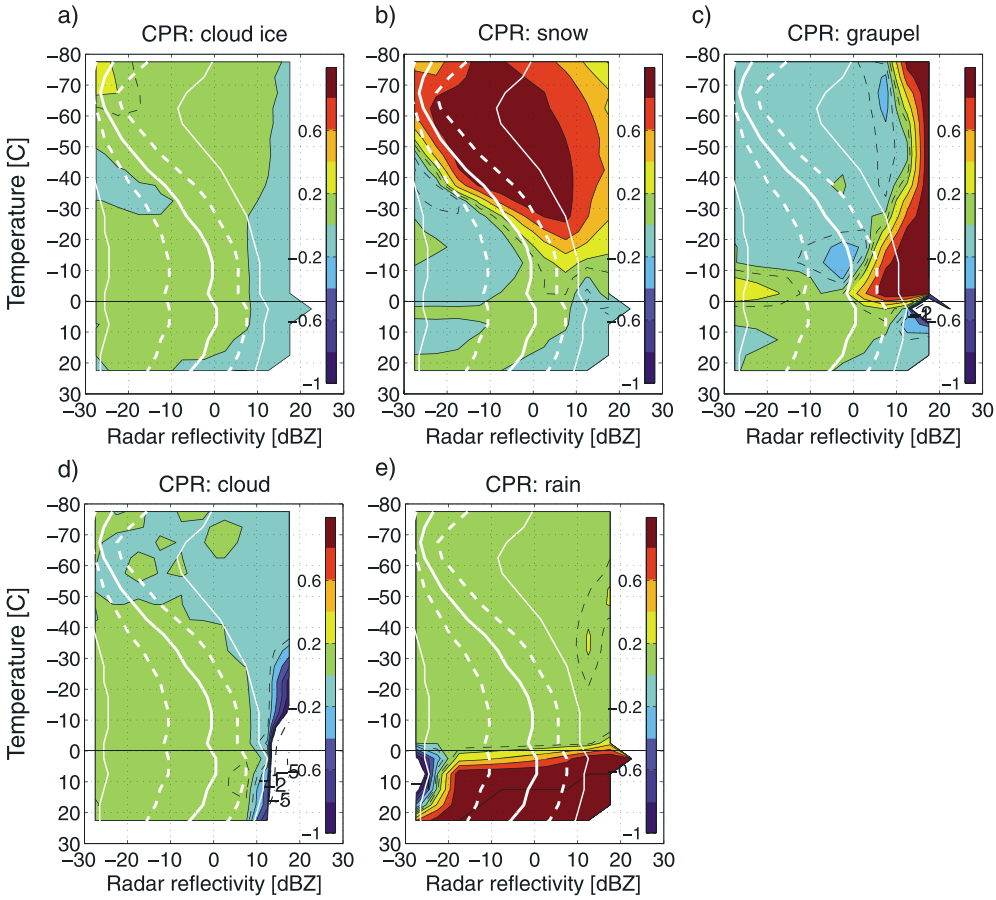

Figure 7. Contribution of hydrometeor categories for global C1 CFED of 95 GHz radar reflectivity. (a) Cloud ice. (b) Snow. (c) Graupel. (d) Cloud water. (e) Rain. White lines mark the 5th, 25th, 50th, 75th, and 95th percentiles as in Figure 5. The black dashed lines indicate 0.1 and −0.1.

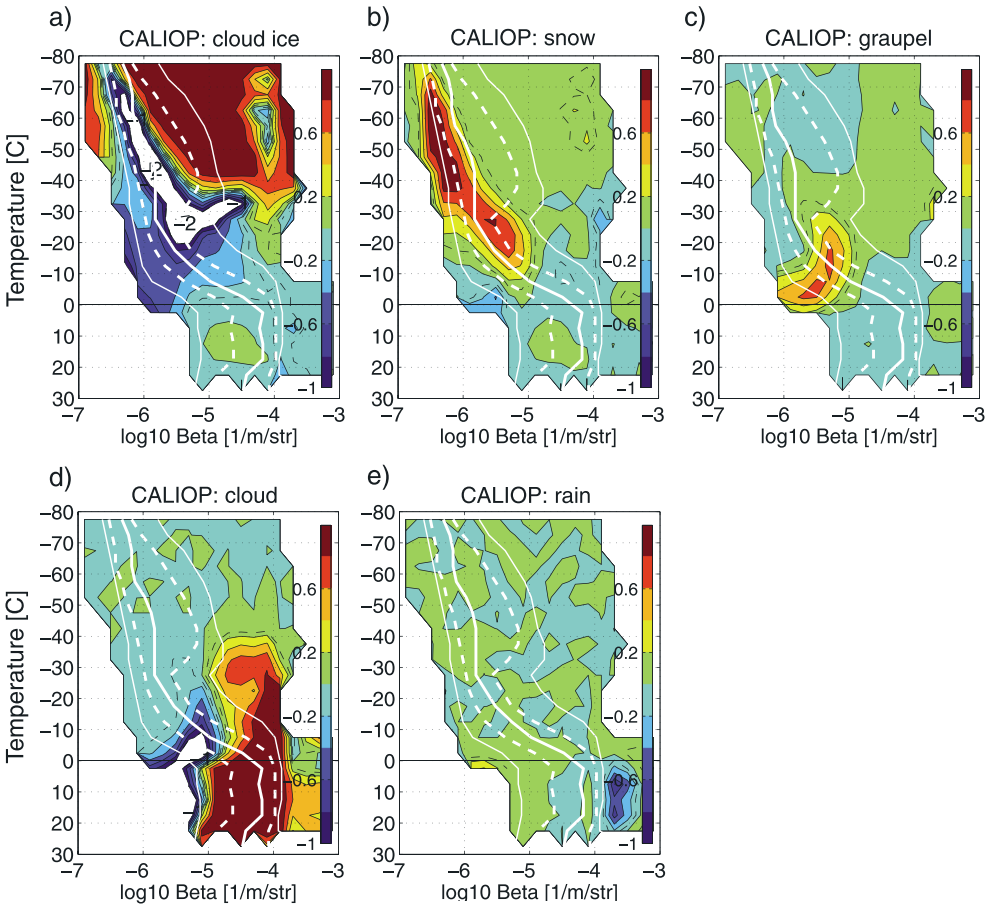

Figure 8. Same as Figure 5 except for global C2 CFED of the 532 nm lidar backscattering coefficient.

by graupel (Figure 7c). The overproduction of graupel relative to snow category or microphysical discontinuity between snow and graupel may be responsible for the change of the mode slope in the CFED of Z_e that does not exist in the observation. Interestingly, graupel contributes to the small Z_e at T above −10°C. Negative contribution of graupel can be seen around −15°C and 0 dBZ and −65°C and 8 dBZ. In cases where multiple categories exist in a grid box, removal of a category with large particles can lead to the increase of samples in the bins of small signals. In this case, snow coexists with graupel. The contribution of liquid particles to the global C1 CFED is limited at T above 0°C (Figures 7d and 7e). Most of the signals associated with precipitation (exceeding −10 dBZ) are related to rain category. The negative contribution by rain and no significant contribution of cloud water suggest that cloud water produces nonprecipitating signals (less than −20 dBZ) but that the occurrences of grid boxes with only cloud water are negligible compared to those with cloud water and rain both present. Cloud water actually negatively contributes to the large Z_e (>10 dBZ). The net signal strength from the hydrometeors that remain can be larger when the excluded hydrometeors attenuate signals more than it adds.

[36] With this diagram, one can easily associate the percentiles with hydrometeor categories. For instance, the 75th and 95th percentiles in Figure 5b are explained mostly by snow at T below −20°C but graupel between −20 and 0°C. However, in some regions, such as that between −30 and 0°C and Z_e less than the median, none of the hydrometeors dominates. Here the signals likely have contributions stemming from multiple categories.

[37] The $C^h(i,k)$ of the C2 CFED of $\log10(\beta_{532})$ is shown in Figure 8. Cloud ice (Figure 8a) indicates a positive contribution at T below −40°C, which corresponds to the large mode in Figure 5d. The large negative contribution at the left of the positive area is because the hydrometeors without cloud ice have small IWC and/or large effective radius. The remaining hydrometeors are likely snow since snow contributes positively for the similar range of β_{532} (Figure 8b). It is now clear that the small mode in Figure 5d is associated with snow-dominant grids. Between −40 and −15°C, snow contributes the most to the C2 CFED, largely determining the median, though graupel (Figure 8c) makes a contribution between −25 and 0°C. In contrast to the C1 CFED of Z_e, cloud water (Figure 8d) explains most of the large signals for T between −35 and 0°C and $\log10(\beta_{532})$ larger than −5. The 95th percentile and higher in the range are explained by cloud water, corresponding to the rare occurrence of supercooled liquid with NSW6 (Figure 5d). The negative contribution between −30 and 0°C suggests coexistence of graupel with cloud water. At T above 0°C, the lidar signals are mostly explained by cloud water (Figure 8d). Rain category causes attenuation, which negatively contributes to $\log10(\beta_{532})$ larger than −4 (Figure 8e)

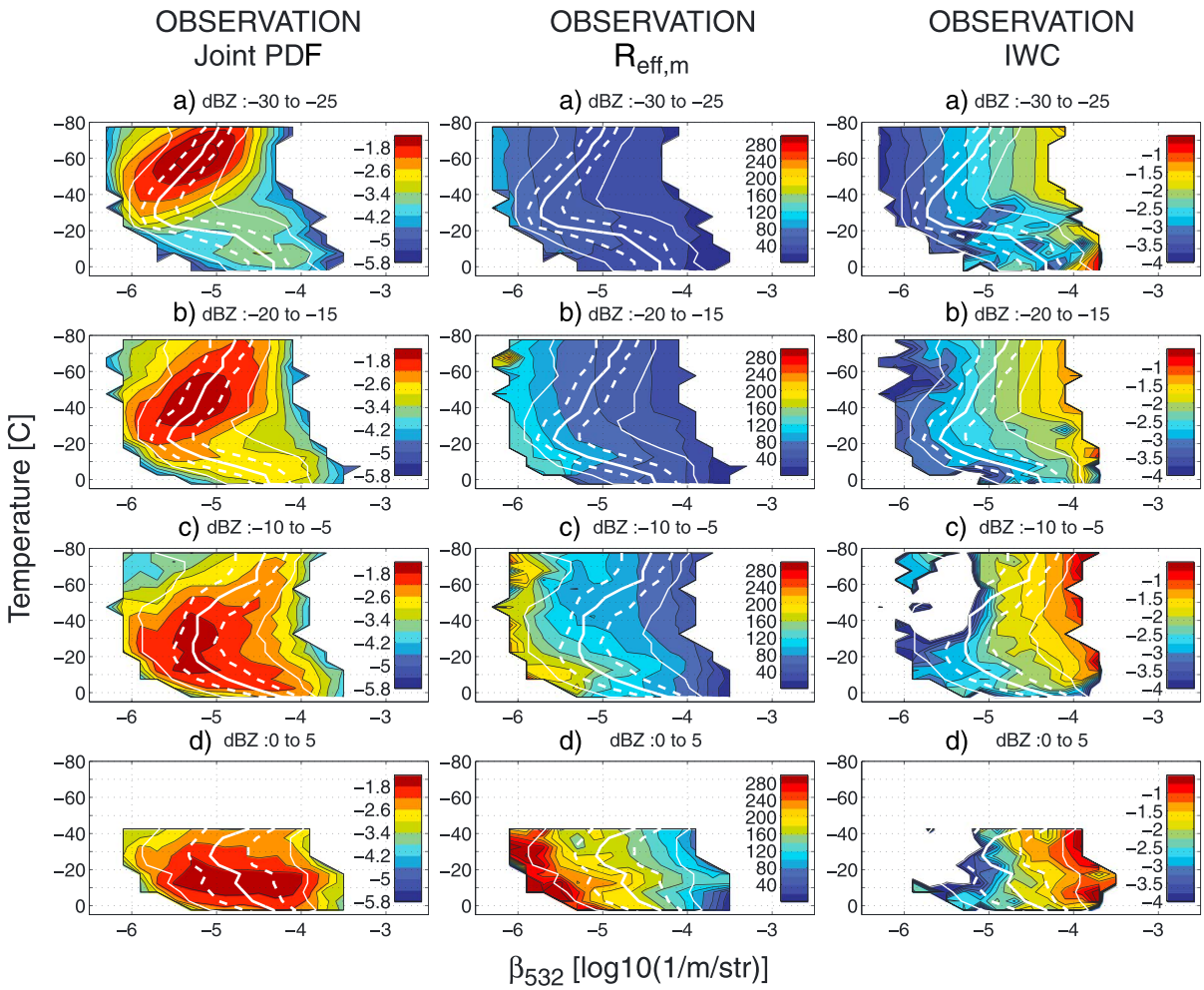

Figure 9. Cloud-top beta-temperature radar-conditioned (CT BETTER) diagram showing the distribution of ice hydrometeor properties at cloud top in the tropics (0°N–15°N). Calculations by CSCA-MD cover temperature, 532 nm lidar backscattering, and 95 GHz radar reflectivity. (left) Joint probability density function; (middle) mean mass-equivalent effective radius; (right) mean water content. Each panel contains samples whose reflectivity is within a range of 5 dBZ. The JPDF scale is logarithmic. The units for effective radius and water content are μm and log10 (g/m^3). The white lines mark 5th, 25th, 50th, 75th, and 95th percentiles.

3.4. Using BETTER to Evaluate the Effective Radius and Water Content

[38] To improve the simulated cloud radiative heating rates and growth processes, we must evaluate profiles of hydrometeor sizes and water content. As the radar reflectivity and lidar backscattering show a different dependence on effective radius for a given water content, it is possible to retrieve two parameters of particle size distributions [e.g., *Donovan and van Lammeren*, 2001; *Okamoto et al.*, 2003]. Following *Okamoto et al.* [2003], we propose a radar-and-lidar method to evaluate simulated water content and effective radius (mass-equivalent effective radius, $R_{\mathrm{eff},m}$, for ice particles) without use of retrievals.

[39] We follow the diagnostic principle in *Okamoto et al.* [2003, Figure 4]:

[40] 1. If Z_e are the same among two grid boxes, smaller β_{532} means larger $R_{\mathrm{eff},m}$.

[41] 2. If Z_e are the same among two grid boxes, larger $R_{\mathrm{eff},m}$ means smaller IWC.

[42] The above consequences are true as long as IWC and β_{532} are monotonically decreasing and unique functions of $R_{\mathrm{eff},m}$ for a given Z_e. If we assume that both the observation and simulation follow the same β_{532}-$R_{\mathrm{eff},m}$ and IWC-$R_{\mathrm{eff},m}$ relationships for a given Z_e, then simulated $R_{\mathrm{eff},m}$ and IWCs can be evaluated by comparing the magnitudes of simulated and observed β_{532} for a given Z_e.

[43] To apply this principle statistically, the samples of radar and lidar signals are first extracted with use of the C3 mask. Then, only samples with ice or liquid particles are extracted with the method described in section 2.3. The samples are further binned in 5 dB increments of Z_e, extending from −30 to 10 dBZ. We assume the 5 dB increment is small enough to satisfy the above logic. Finally, the JPDF of T and β_{532} can be constructed for each Z_e bin.

[44] We first examine the JPDF at 5 dB increment of Z_e bin for the observed ice hydrometeors at cloud top, hereafter a CT BETTER (cloud-top beta-temperature radar-conditioned) diagram. To avoid ambiguity in interpretation of different

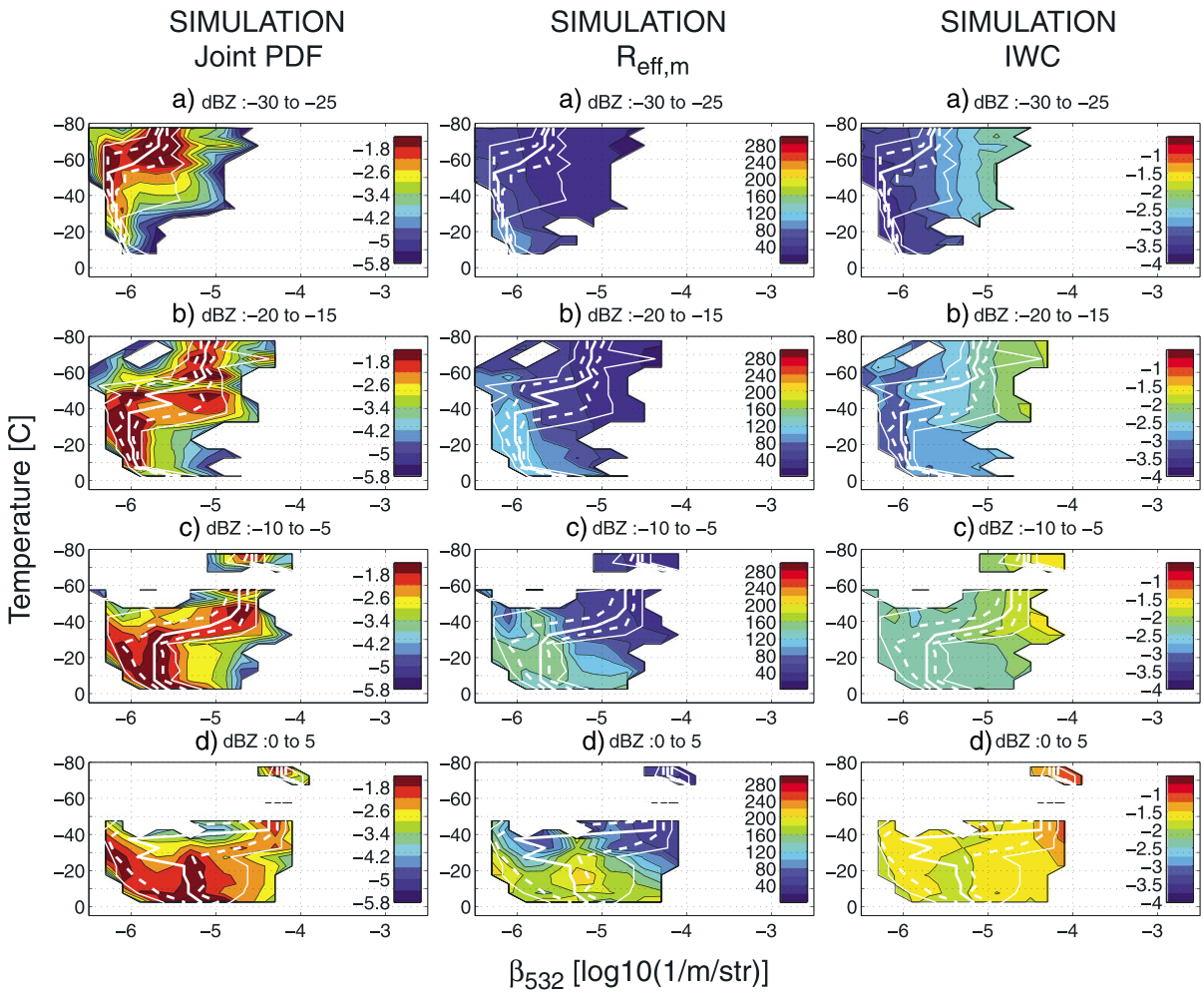

Figure 10. Same as Figure 9 except simulated from NICAM.

cloud types, we focus on the samples in the tropics (0°N–15°N) (see Figure 1 for the C3 cloud tops). The white solid and dash curves shown in the CT BETTER diagrams of Figure 9 (left column) are the 5th, 25th, 50th, 75th, and 95th percentiles for each bin of T. They show that the dominant mode shifts to warmer T with increasing Z_e as expected from the C1 CFED of Z_e. The middle and right columns of Figure 9 show the mean retrieved $R_{\mathrm{eff},m}$ and IWC, respectively. For a given Z_e bin, when β_{532} increases, $R_{\mathrm{eff},m}$ decreases on average, whereas IWC increases on average. Conversely, for a given T and β_{532}, as Z_e increases, both $R_{\mathrm{eff},m}$ and IWC increase. The above diagnostic principle applied to $R_{\mathrm{eff},m}$ and IWC are valid over the Z_e at a fixed T. But, as indicated by the rapid change of the mean $R_{\mathrm{eff},m}$ and IWC at warmer T, the principle may not be valid over T for a fixed Z_e. For a 5 dB increment of Z_e, for instance, for −20 to −15 dBZ, the above diagnostic principle suggests that the negative slope of the median β_{532} is related to the increase in $R_{\mathrm{eff},m}$ (or decrease in IWC) with increasing T. Indeed, the mean $R_{\mathrm{eff},m}$ and IWC support this diagnostic principle. The slope around the mode changes from a negative to a positive one with Z_e. We speculate that this is because for large Z_e the increase of IWC with T is so large that $R_{\mathrm{eff},m}$ has to decrease to achieve the same Z_e.

[45] Now we compare the simulated β_{532} against observation to evaluate the simulated $R_{\mathrm{eff},m}$ and IWC indirectly (compare left columns of Figures 9 and 10). The evaluation should be similar to applying the retrieval scheme to the simulated signals with the mean projection shown in the middle and right columns of Figure 9. Comparison of two modes in the simulated JPDF for −30 to −25 dBZ and T below −40°C (Figure 10, left column) indicates that the cloud tops forming the mode of log10(β_{532}) near −6.2 (in units log10 of 1/m/str) have a larger $R_{\mathrm{eff},m}$ and smaller IWC than those of log10(β_{532}) near −5.6. Compared to the mode of log10(β_{532}) around −5.2 in the observed JPDF (Figure 9, left column), the simulated cloud tops with these modes overestimate $R_{\mathrm{eff},m}$ and underestimate IWC. The analysis in section 3.3 indicates that the small mode corresponds to snow category, while the cloud tops with cloud ice dominant form the large mode. The simulated cloud tops for −20 to −15 dBZ show further separation of the signals contributed by the two categories. In this range, the agreement between the simulated and observed modes suggests that $R_{\mathrm{eff},m}$ and IWC of cloud ice category are in a good agreement with the observation. For −10 to −5 dBZ, the contribution from cloud ice remains in the large mode (~4.7) at T below −35°C, whereas snow and graupel categories

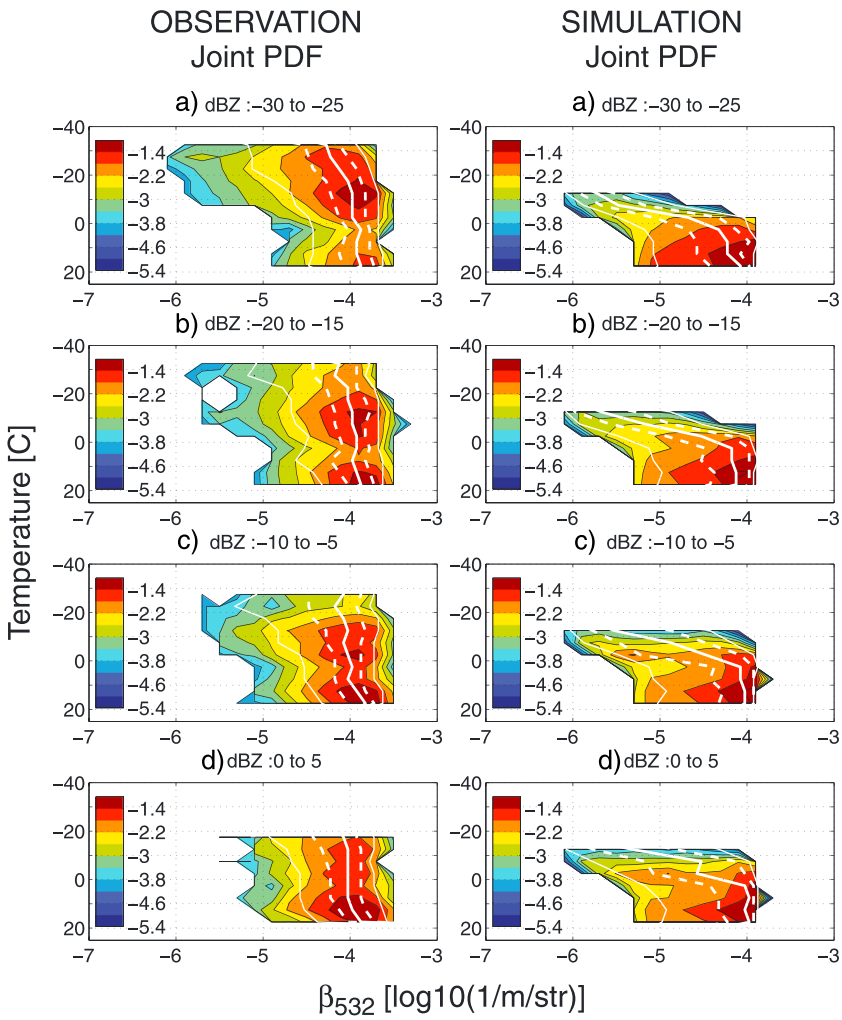

Figure 11. Joint probability density function over temperature, 532 nm lidar backscattering, and 95 GHz radar reflectivity at cloud top in the tropics (0°N–15°N). (left) For liquid hydrometeors, calculated with CSCA-MD. (right) The same except simulated from NICAM.

contribute to the other modes. Based on the vertical profiles of signals (Figure 1), we speculate that the large mode related to cloud ice is associated with the deep convective cloud tops. Comparing $\log10(\beta_{532})$ at the probability density of more than $10^{-1.8}$ (dark red fill), the simulation tends to overestimate $R_{\mathrm{eff},m}$ but underestimate IWC at T above −35°C. For 0 to 5 dBZ, the frequency at T larger than −10°C (T less than −10°C) is mostly explained with graupel (snow) category (Figure 7). The observation has a high probability density for $\log10(\beta_{532})$ exceeding −5, implying that the simulation underestimates (overestimates) IWC ($R_{\mathrm{eff},m}$). We infer that the separation of the two modes at Z_e above −10 dBZ and T above −35°C is associated with different growth regimes: the small mode with stratiform cloud layers and large mode with convective cloud layers.

[46] Comparison of the middle and right columns of Figures 9 and 10 indicates that at Z_e below −15 dBZ, the relationship between the signals and microphysical variables

Table 3. Relative Frequency of the Radar Reflectivity for Radar-and-Lidar Mask Used in BETTER for Cloud Tops With Ice Particles[a]

Z_e Range [dBZ]		Observation	Control	Cloud Ice R_{eff} = 20 μm	Snow N_0 = 0.1 cm^{-4}	Snow N_0 = 10 cm^{-4}
−30	−25	49.56	78.07	77.37	80.90	83.00
−25	−20	23.80	9.65	9.61	8.93	9.31
−20	−15	10.89	4.81	5.02	4.11	3.59
−15	−10	6.80	3.11	3.34	2.66	1.89
−10	−5	4.23	2.20	2.38	1.77	1.13
−5	0	2.64	1.34	1.43	0.99	0.65
0	5	1.49	0.62	0.65	0.47	0.32
5	10	0.60	0.20	0.20	0.16	0.11
Sample size		461,059	2,648,427	2,555,932	2,309,564	1,549,306

[a]The samples were taken in the tropics (between 0°N and 15°N).

Table 4. Same as Table 3 Except for Liquid Particles

Z_e Range [dBZ]		Observation	Control	Cloud Water $R_{\mathrm{eff}} = 11\ \mu\mathrm{m}$
−30	−25	13.37	11.69	10.63
−25	−20	22.75	11.00	10.95
−20	−15	18.81	11.25	11.89
−15	−10	17.36	12.75	13.19
−10	−5	12.47	14.24	14.31
−5	0	7.76	15.02	14.78
0	5	4.76	13.78	13.64
5	10	2.72	10.27	10.61
Sample size		67,436	671,258	355,699

in the NICAM simulation qualitatively resembles that of the observation. In this case, the diagnosis with signals (forward approach) leads to a similar result obtained by comparing retrieved and simulated $R_{\mathrm{eff},m}$ and IWC (inversion approach). However, in the regime of Z_e exceeding −15 dBZ and log10 (β_{532}) below −5, differences in the relationship are evident, which means that forward and inversion approach give different diagnoses on the simulated $R_{\mathrm{eff},m}$ and IWC. In the simulation, for 0 to 5 dBZ, the monotonic change in mean $R_{\mathrm{eff},m}$ and IWC with log10(β_{532}) does not hold at log10 (β_{532}) below −5. This probably corresponds to the fact that the PSDs of the NICAM simulation can be multimodal or the small end of the PSDs does not affect the IWC but does the $R_{\mathrm{eff},m}$. In addition, the simulation underestimates the mean $R_{\mathrm{eff},m}$, not reaching the retrieval values that exceed 220 µm. In general, the differences in the relationship between signals and microphysical variables can be attributed to crystal habits (mass-dimensional relationships), the number of categories, and the PSDs assumed in the retrievals and the microphysical scheme. Without having direct particle measurements, one should do the comparison with the signal and microphysical parameters.

[47] The above diagnostic principle is a quick way to statistically evaluate $R_{\mathrm{eff},m}$ and IWC at cloud top. It can also be applied to individual vertical profiles such as those shown in Figure 2. Here observed and simulated cloud tops have a similar range of Z_e (less than −20 dBZ), but simulations underestimate log10(β_{532}), and mostly take on values between −6 and −5.2. These two values correspond to the separated modes shown in the left column of Figure 10, which exist also in the midlatitudes. The diagnostic principle suggests that the simulation overestimates $R_{\mathrm{eff},m}$ but underestimate

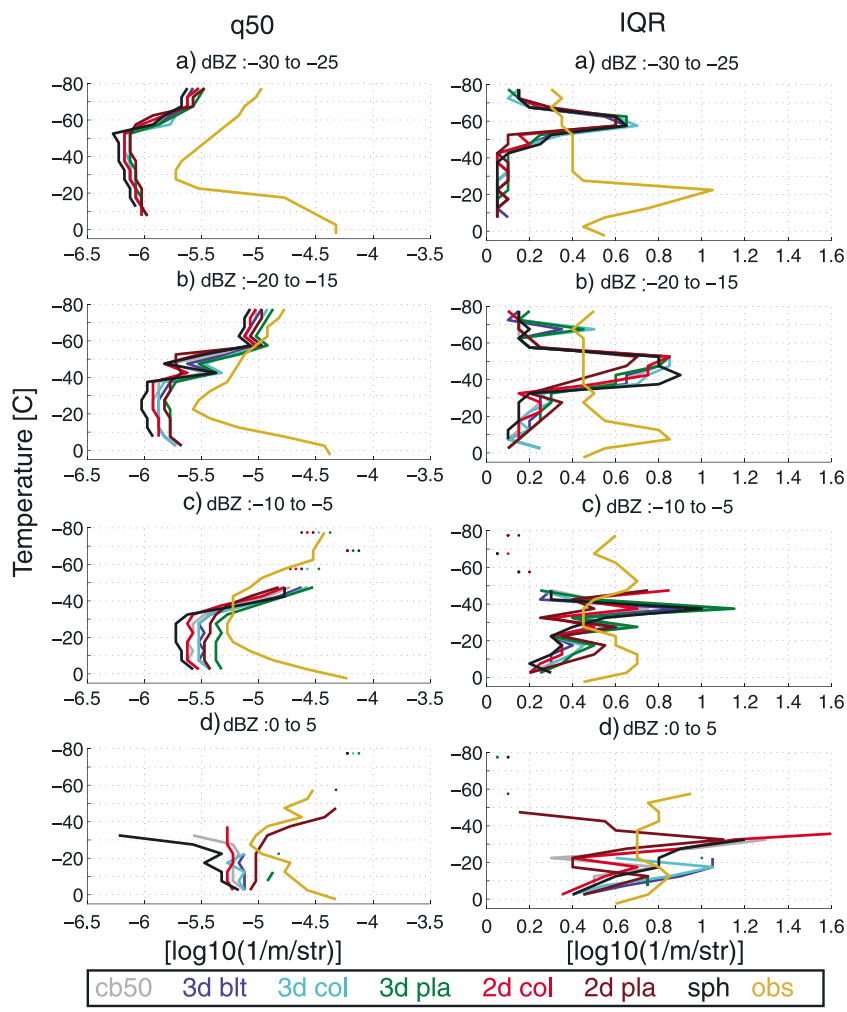

Figure 12. Comparison of percentiles simulated with nonspherical ice scattering tables for CT BETTER in the tropics (between 0°N and 15°N). (left) The median of lidar backscattering coefficient for ranges of radar reflectivity; (right) the IQR = q75–q25.

IWC for snow and cloud ice at cloud top. As discussed in section 3.1, the simulated infrared T_b tends to underestimate observation by about 10 K or the effective emission height for the deep cloud tends to be lower by about 1.3 km. These relations occur because the optical depth is smaller due to the larger $R_{\mathrm{eff},m}$ and smaller IWC at cloud top.

[48] A CT BETTER for liquid hydrometeors was constructed in the same way as that for ice (Figure 11). As a first approximation, we assume that the same diagnosis can be drawn from β_{532} and Z_e. For each range of Z_e, the observed JPDF has a mode ($>10^{-1.4}$, dark red fill) at T near -10, 0, or 15°C (left column of Figure 11). The mode at 15°C is related to shallow cumulus, whereas the others relate to cumulus congestus. The probability density at T below -20°C increases as the Z_e decreases from Figures 11d to Figure 11a, which may occur because the freezing and riming processes are less likely for the small cloud droplets. The dominant mode of $\log10(\beta_{532})$ remains in the range of -4 to -3.7, irrespective of Z_e, indicating R_{eff} and liquid water content (LWC) tend to increase with Z_e for the modes.

[49] For the simulated liquid hydrometeors, the CT BETTER shows a narrower distribution over T due to underprediction of supercooled droplets (right panel of Figure 11). It does not exhibit the multiple modes over T as seen in the observation, but it does show multiple modes over β_{532} for Z_e larger than -10 dBZ. The mode at $\log10(\beta_{532})$ less than -5 around $T=0$°C is likely related to rain-dominant grids. Over the entire Z_e range, the modes for simulated $\log10(\beta_{532})$ are smaller than that of observation, which suggests that the liquid categories in NSW6 do not capture the occurrences of the small R_{eff} and large LWC as frequently as observations.

[50] Comparison of the occurrences of Z_e ranges used for the BETTER provides further information on the model biases discussed above. Table 3 shows the relative frequency of the Z_e for cloud tops with ice particles that were identified with the C3 mask. The simulation (control) has 78% of the samples concentrated in the smallest Z_e range, whereas more samples are distributed toward the tail for the observed Z_e. This means that the simulated clouds defined with the C3 mask are dominated by ice particles with small sizes or small IWC. As for the liquid particles (Table 4), the simulation underestimates the relative occurrence of the nonprecipitating cloud tops ($Z_e < -20$ dBZ). On the other hand, the simulated precipitation-probable cloud tops ($-10 < Z_e$ dBZ) is overpredicted. It suggests that the autoconversion of cloud water is too efficient in the simulation. *Suzuki et al*. [2011] also reported that another cloud microphysics scheme of NICAM as well as that of RAMS converts cloud water to larger-sized particles more quickly than the CloudSat-MODIS analysis indicates.

[51] The diagnosis of IWC and size with BETTER diagram is somewhat sensitive to the ice scattering model used. Figure 12 shows the median (left column) and IQR (right column) calculated with the seven ice scattering models in the CT BETTER diagram corresponding to Figure 10. The spread of median β_{532} as well as IQR among the ice models increases with Z_e. The peaks in the IQRs for the simulation, such as one at $T=-60$°C for -30 to -25 dBZ, are related to the transition from one to the other mode as seen in Figure 10. For Z_e less than -5, the qualitative relation between the simulated and observed medians remains mostly the same, irrespective of the ice models. The IWC ($R_{\mathrm{eff},m}$) of ice particles tends to be underestimated (overestimated) except for T below -40°C for -10 to -5 dBZ. For the largest Z_e range, the use of the 2-D plate produces the observed median between -30 and -40°C, while the ice sphere case indicates the median decreasing toward -30°C. This is because the medians of the sphere and 2-D plate follow the small and large modes associated with snow and cloud ice dominant grids, respectively. Thus, the diagnosis can be uncertain for the large Z_e ranges where the variability of Z_e becomes large.

4. Discussion

[52] In this section, we discuss links between the characteristics of the simulated signals and the parameters of the bulk microphysical scheme (NSW6). The sensitivity of the signals to the microphysical parameters (see Table 2) is explored in the forward calculation only. For each sensitivity test, only one parameter is changed with the others remaining the same as the control. Note that the goal of this sensitivity analysis is only to provide a first-order estimate of the effects that changes in the microphysical parameterization might have on the radar and lidar signals through CT BETTER diagrams. The dynamical and thermodynamical feedbacks on the microphysics are likely to change the signals significantly.

4.1. Cloud Ice

[53] According to the CT BETTER diagnosis, $R_{\mathrm{eff},m}$ and IWC of cloud ice dominant grids produce the observed mode of $\log10(\beta_{532})$ near -5.2 (in log10 of 1/m/str) for -20 to -15 dBZ (Figure 9, left column). To see the effectiveness of a CT BETTER, the cloud ice R_{eff} in the simulated signals was reduced to a constant R_{eff} of 20 μm in the Joint-Simulator. We compare the result against the control with R_{eff} equal to 40 μm (Figure 10, left column). The resulting mass content of cloud ice (Figure 13, left column) is still the same as the control. As R_{eff} decreases from 40 to 20 μm, the large modes related to grids with cloud ice dominant are shifted to larger $\log10(\beta_{532})$ by about 0.2. Correspondingly, for all the Z_e ranges, the $R_{\mathrm{eff},m}$ and IWC values averaged in the $T-\log10(\beta_{532})$ space are shifted toward larger β_{532} (not shown). As a result, the large mode for -30 to -25 dBZ matches with the observation. These changes occur because the smaller $R_{\mathrm{eff},m}$ of cloud ice dominant grids leads to larger $\log10(\beta_{532})$ for a fixed IWC, but its effect on the Z_e is very limited, and coexisting snow is responsible for determining the Z_e (Figure 7a). This point is supported by the relative frequency of Z_e (Table 3), which is little changed from control. Thus, the small R_{eff} of cloud ice improves only the lidar signals for some Z_e range, and CT BETTER can be used to evaluate the assumed R_{eff} of cloud ice.

4.2. Snow

[54] Below -30°C, the simulated lidar signal shows the two modes as seen in Figure 5d and the left column of Figure 10. In NSW6, cloud ice converts to snow through the autoconversion term $P_{SAUT}=\beta_1\,(q_i-q_{icrt})$. The value of q_{icr} is set to 0 for this experiment, which may overproduce snow of small ice water contents for T below -30°C. The snow PSD in NSW6 is given by the Marshall-Palmer

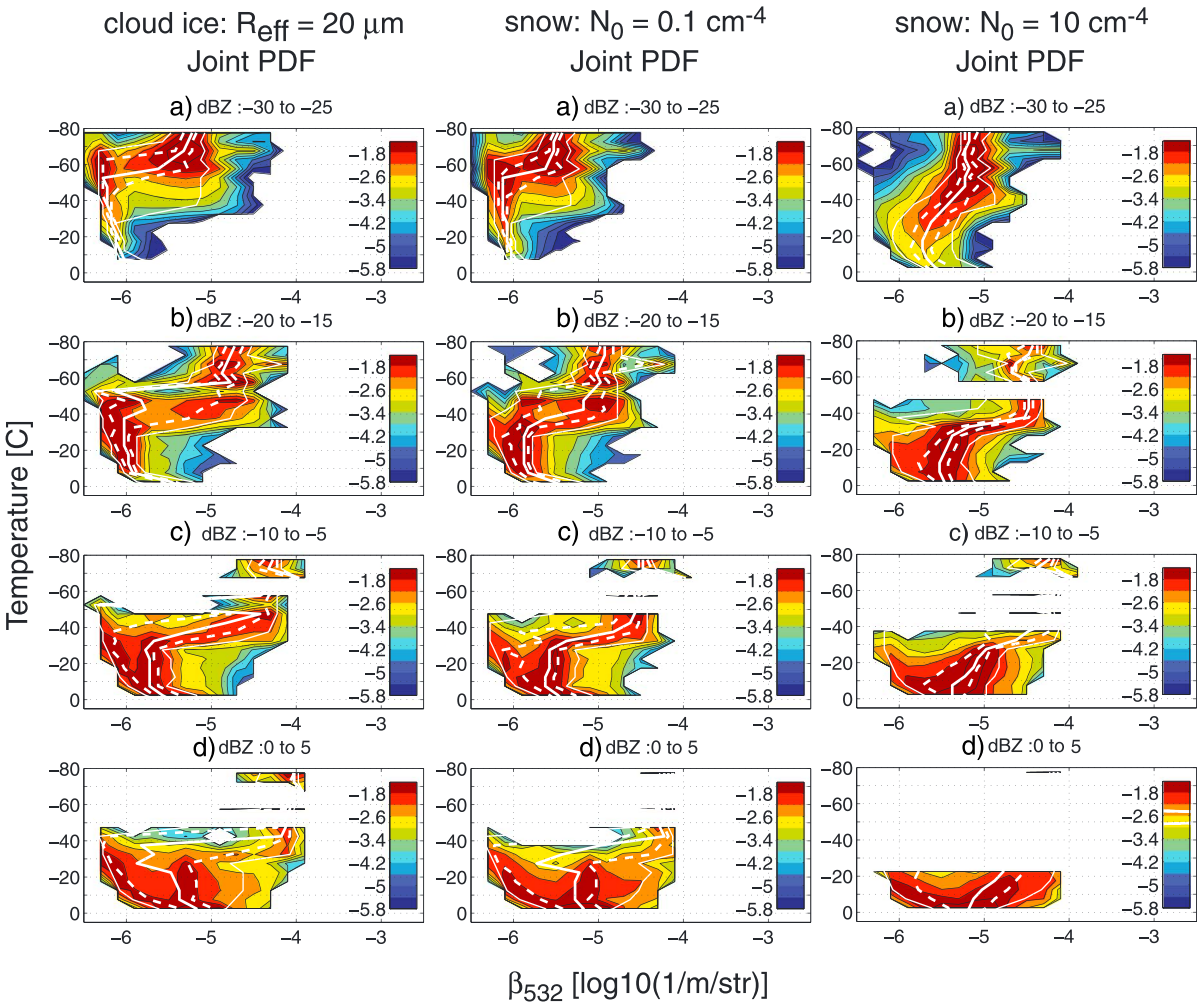

Figure 13. Joint probability density function over temperature, 532 nm lidar backscattering, and 95 GHz radar reflectivity at cloud top in the tropics (between 0°N and 15°N). (left) Cloud ice with R_{eff} set to 20 μm. Snow with (middle) $N_0 = 0.1\ \mathrm{cm}^{-4}$ and (right) $N_0 = 10\ \mathrm{cm}^{-4}$.

distribution $N(D) = N_0 \exp(-\lambda D)$, where N is the number concentration per size, N_0 is the intercept parameter, λ is the slope parameter, and D is the maximum dimension. At a fixed IWC, when N_0 increases, λ increases and the R_{eff} of snow decreases. The control setting uses $N_0 = 0.03\ \mathrm{cm}^{-4}$, which corresponds to the correct value for cloud bottom, according to the aircraft observations of deep tropical cirrus and stratiform clouds by *Heymsfield et al.* [2002]. The small value of N_0 at the high levels is not realistic for deep stratiform clouds and thus may lead to oversized snow particles that fall before accreting cloud ice. *Masunaga et al.* [2008] also found that another simple bulk microphysics scheme of NICAM overestimated the fraction of large snowflakes by using the TRMM PR and CloudSat CPR.

[55] The CT BETTER analysis showed that the simulations with the C3 mask overestimates $R_{eff,m}$ and underestimated IWC of snow at cloud top. To see the sensitivity of the signals on N_0, CT BETTER diagrams were constructed for $N_0 = 0.1\ \mathrm{cm}^{-4}$ and $N_0 = 10\ \mathrm{cm}^{-4}$ (Figure 13, middle and right). According to *Heymsfield et al.* [2002], these values correspond to about 5 K above cloud bottom and around cloud top, respectively. For $N_0 = 0.1\ \mathrm{cm}^{-4}$, the mode of small β_{532} in the JPDF, or the median at T below −10°C, shifts to the larger value. This shift is expected from having a smaller R_{eff} than the control. For the larger N_0 case (=10 cm^{-4}), the mode associated with snow category further shifts to the larger β_{532}. For −30 to −25 dBZ, the modes no longer separate because the snow particles producing the small mode now are smaller, resulting in a smaller Z_e. Also, for −20 to −15 dBZ, the mode between −10 and −30°C agrees better with the observation. Although an increase of N_0 may improve the simulated β_{532} at cloud top, the increase reduces the occurrence of radar-observed cloud layers in the sample size, and the relative frequency of the Z_e may not be improved at all (Table 3). In reality, N_0 and λ or moments for aggregation-dominant PSDs are known to depend on T and IWC [e.g., *Heymsfield et al.*, 2002; *Field et al.*, 2005]. Inclusion of such relationships can be tested with BETTER to some extent.

[56] The same sensitivity analyses for 19 June at 12:00Z were done using the broadband simulator (MSTRNX) for the top-of-atmosphere (TOA) longwave upwelling fluxes. In the tropics (30°S–30°N), the fluxes for the control case, the case of cloud ice with $R_{eff} = 20$ μm, snow with $N_0 = 0.1\ \mathrm{cm}^{-4}$, and snow with $N_0 = 10\ \mathrm{cm}^{-4}$ are 252.8, 243.9, 251.8, and 244.4 Wm^{-2}, respectively. This implies

the parameterization of the snow PSD can affect the TOA energy budget as much as that of cloud ice.

4.3. Cloud Water

[57] As shown by CT BETTER (Figure 11), the simulation underestimates the water content but overestimates R_{eff} of the liquid hydrometeors. The R_{eff} of cloud water category (16 μm) is too large compared to the annual zonal mean that is estimated with the Advanced Very High Resolution Radiometer (AVHRR) [*Kawamoto et al.*, 2001]. For warm clouds off the coast of California, the R_{eff} retrieved with AVHRR shows a mode near 11 μm [*Nakajima and Nakajima*, 1995; *Sato et al.*, 2012]. For single-layer mixed-phase clouds in the Arctic, a lidar-radar retrieval algorithm gives mean R_{eff} of 12 μm [*de Boer et al.*, 2009]. The signals simulated with R_{eff} set to 11 μm shift the mode slightly to larger values but do not significantly increase the number of samples with $\log10(\beta_{532})$ above -4 (not shown). This suggests that the water content of cloud water has to be increased. The decrease of R_{eff} of cloud water does not affect the relative frequency of Z_e (Table 4), as in the case for cloud ice, and the distribution of Z_e is mainly determined by rain category. Making the autoconversion of cloud water slower may increase the nonprecipitating samples and the water content of cloud water, which possibly improves both of the lidar and radar signals.

5. Summary

[58] This study demonstrated an effective way to evaluate cloud microphysics simulated by a global CRM against CloudSat and CALIPSO measurements. The signals from ice particles were calculated with Mie approximation, assuming ice sphere. Firstly, we investigated the vertical profiles of a tropical cyclone and a midlatitude frontal system, which allowed us to better understand the horizontal and vertical characteristics of clouds as well as dependence of the signal biases on the cloud systems. The simulated signals possess the characteristics typically seen in convective and stratiform clouds. However, the simulated upper clouds tend to be optically thinner for both the systems. The tropical system has more isolated convective cells with less stratiform portion, while high values of reflectivity (>10 dBZ) was barely found in the midlatitude profiles.

[59] Secondly, we evaluated the global in-cloud statistics of the radar and lidar signals. By switching off the input of each hydrometeor category, we could determine the contribution of each hydrometeor to the simulated signals. The CFED (contoured frequency by temperature diagram) for the observed Z_e had a clear temperature dependence of the probability density with the global samples. The NICAM simulation also showed such a dependency but with a tighter spread of samples and the mode shifted toward colder T. The NICAM simulation overestimated all the percentiles at T above -50°C. Interestingly, the mode below -20°C is mostly explained with snow and cloud ice only contributes to the small Z_e (below -20 dBZ) between -80 and -65°C. Below -35°C, the CFED for the simulated β_{532} had two modes associated with cloud ice and snow in the model, though observations had only one mode. Above -40°C, cloud water explained most of the large β_{532} range where $\log10(\beta_{532})$ exceeded -5. It is attributed to underestimation of the 75 and 95th percentiles.

[60] As the third step, we tested the effective radius and water content at the radar-and-lidar-defined cloud tops against observation. The diagnostic principle followed the basic theoretical relation embedded in the radar-and-lidar retrieval scheme of *Okamoto et al.* [2003]: for cloudy grids with the same Z_e, larger β_{532} means smaller $R_{\mathrm{eff},m}$ and larger IWC. In order to apply the retrieval principle, the samples of β_{532} were separated into liquid and ice cloud top and then grouped by Z_e. These were called cloud-top (CT) BETTER. The simulated β_{532} contributed by snow category tended to be lower than the observations over all $Z_{e,}$, which indicates that the simulation underestimates IWCs but overestimates $R_{\mathrm{eff},m}$ of snow at cloud top. The β_{532} of cloud ice dominant grids agreed well with observations between -20 and -15 dBZ, but the IWCs ($R_{\mathrm{eff},m}$) above the deep convective core were likely overestimated (underestimated). Furthermore, the liquid CT BETTER suggested that the simulations had too small a cloud water content and too efficient a conversion of cloud water to rain. We found that CT BETTER diagrams are useful to understand the relationships between the simultaneous radar and lidar signals and cloud microphysical parameters in NICAM.

[61] Whichever inversion or forward approach is used, it is critical to evaluate the uncertainty in the diagnosis. Six nonspherical ice scattering models were utilized to assess the potential impacts. Although use of 2-D plate model can produce the signals comparable to the observation, we are not suggesting this is an appropriate model to use in the radar simulator for all ice clouds, given the limited temperature range that this particle type is expected to exist in the real atmosphere. Rather, the point is that the model underestimates IWC, and using a 2-D plate model compensates for this underestimation to some degree. For the global CFEDs, the spreads of the signals calculated with the nonspherical scattering models were about a half of the spreads associated with particle size distributions. Fortunately, the differences in the statistics between the simulation and observation remain qualitatively similar among all the scattering models for this simulation. The BETTER diagnosis of IWC and size was found somewhat uncertain for the large Z_e range.

[62] The above analyses raised the following important issues. The BETTER revealed that the mean cloud microphysical quantities from the model and retrieval for a given pair of radar and lidar signals can be qualitatively different. This illustrates that the long-standing differences in the microphysical assumption between models and retrievals still remain. For the effective implementation of the statistical radar-and-lidar evaluation, we need to first improve the upper level cloud occurrences. We applied BETTER diagrams only to cloud tops, but the method can be applied to any level reached by the lidar from above. For clouds that are not defined by the cloud mask, another approach is necessary to evaluate water content and particle size of the clouds. The microphysical growth processes are embedded in BETTER diagrams as the relationships among temperature and radar and lidar signals. However, this paper could not give an interpretation especially on the ice growth processes. Additional physical insights may be obtained once BETTER is organized by cloud or atmospheric types. Also, if we are to improve global CRMs in the context of climate prediction, it

is important to link the evaluation of water content and particle size to the evaluation of energy budgets and surface precipitation.

[63] **Acknowledgments.** This research was supported by the JAXA/EarthCARE 1st Research Announcement. We thank Chihiro Kodama and Alessandro Battaglia for valuable discussions, leading to a better manuscript. We also appreciate the valuable comments and suggestions by the anonymous reviewers. The NICAM simulations were done using the Earth Simulator at the Japan Agency for Marine-Earth Science and Technology (JAMSTEC).

References

Battaglia, A., T. Augustynek, S. Tanelli, and P. Kollias (2011), Multiple scattering identification in spaceborne W-band radar measurements of deep convective cores, *J. Geophys. Res.*, *116*, D19201, doi:10.1029/2011JD016142.

Bodas-Salcedo, A., M. J. Webb, M. E. Brooks, M. A. Ringer, K. D. Williams, S. F. Milton, and D. R. Wilson (2008), Evaluating cloud systems in the Met Office global forecast model using simulated CloudSat radar reflectivities, *J. Geophys. Res.*, *113*, D00A13, doi:10.1029/2007JD009620.

Bodas-Salcedo, A., et al. (2011), COSP: Satellite simulation software for model assessment, *Bull. Am. Meteorol. Soc.*, *92*, 1023–1043, doi:10.1175/2011BAMS2856.1.

de Boer, G., E. W. Eloranta, and M. D. Shupe (2009), Arctic mixed-phase stratiform cloud properties from multiple years of surface-based measurements at two high-latitude locations, *J. Atmos. Sci.*, *66*, 2874–2887.

Donovan, D. P., and A. C. A. P. van Lammeren (2001), Cloud effective particle size and water content profile retrievals using combined lidar and radar observations: 1. Theory and examples, *J. Geophys. Res.*, *106*, 27425–27448, doi:10.1029/2001JD900243.

Eito, H., and K. Aonashi (2009), Verification of hydrometeor properties simulated by a cloud-resolving model using a passive microwave satellite and ground-based radar observations for a rainfall system associated with the Baiu front, *J. Meteorol. Soc. Jpn.*, *87*, 425–446.

Field, P. R., R. J. Hogan, P. R. A. Brown, A. J. Illingworth, T. W. Choularton, and R. J. Cotton (2005), Parameterization of iceparticle size distributions for mid-latitude stratiform cloud, *Q. J. R. Meteorol. Soc.*, *131*, 1997–2017.

Gelsthorpe, R. V., A. Heliere, A. Lefebvre, J. Lemanczyk, E. Mateu, and K. Wallace (2008), EarthCARE and its payload, Proc. SPIE, 7157207-1–715207-12.

Hagihara, Y., H. Okamoto, and R. Yoshida (2010), Development of a combined CloudSat-CALIPSO cloud mask to show global cloud distribution, *J. Geophys. Res.*, *115*, D00H33, doi:10.1029/2009JD012344.

Han, M., S. A. Braun, W. S. Olson, P. Ola, G. Persson, and J.-W. Bao (2010), Application of TRMM PR and TMI measurements to assess cloud microphysical schemes in the MM5 for a winter storm, *J. Appl. Meteorol. Climatol.*, *49*, 1129–1148.

Han, M., S. A. Braun, T. Matsui, and C. R. Williams (2013), Evaluation of cloud microphysics schemes in simulations of a winter storm using radar and radiometer measurements. *J. Geophys. Res.*, *118*, 1401–1419, doi:10.1002/jgrd.50115.

Heymsfield, A. J., A. Bansemer, P. R. Field, S. L. Durden, J. L. Stith, J. E. Dye, W. Hall, and C. A. Grainger (2002), Observations and parameterizations of particle size distributions in deep tropical cirrus and stratiform precipitating clouds: Results from in situ observations in TRMM field campaigns, *J. Atmos. Sci.*, *59*, 3457–3491.

Houze, R. A., P. V. Hobbs, P. H. Herzegh, and D. B. Parsons, (1979), Size distributions of precipitation particles in frontal clouds, *J. Atmos. Sci.*, *36*, 156–162.

Ishimoto, H., and K. Masuda (2002), A Monte Carlo approach for the calculation of polarized light: Application to an incident narrow beam, *J. Quant. Spectrosc. Radiat. Transfer*, *72*, 467–483.

Kawamoto, K., T. Nakajima, and T. Y. Nakajima (2001), A global determination of cloud microphysics with AVHRR remote sensing, *J. Clim.*, *14*, 2054–2068.

Kimura, T., H. Nakatsuka, K. Sato, Y. Sakaide, Y. Seki, K. Okada, N. Takahashi, Y. Ohno, and H. Horie (2010), EarthCARE mission with Japanese Space Borne Doppler Cloud Radar; CPR, paper presented at International Society for Photogrammetry and Remote Sensing (ISPRS) Technical Commission VIII Symposium, Kyoto, Japan.

Klein, S. A., and C. Jakob (1999), Validation and sensitivities of frontal clouds simulated by the ECMWF model, *Mon. Weather Rev.*, *127*, 2514–2531.

Kodama, C., A. T. Noda, and M. Satoh (2012), An assessment of the cloud signals simulated by NICAM using ISCCP, CALIPSO, and CloudSat satellite simulators, *J. Geophys. Res.*, *117*, D12210, doi:10.1029/2011JD017317.

Kollias, P., and B. Albrecht (2005), Why the melting layer radar reflectivity is not bright at 94 GHz, *Geophys. Res. Lett.*, *32*, L24818, doi:10.1029/2005GL024074.

Kulie, M. S., R. Bennartz, T. J. Greenwald, Y. Ghen, and F. Weng (2010), Uncertainties in microwave properties of frozen precipitation: Implications for remote sensing and data assimilation, *J. Atmos. Sci.*, *67*, 3471–3487.

Li, X., W.-K. Tao, T. Matsui, C. Liu and H. Masunaga (2010), Improving a spectral bin microphysical scheme using TRMM satellite observations, *Q. J. R. Meteorol. Soc.*, *136*, 382–399.

Lin, Y. L., R. D. Farley, and H. D. Orville (1983), Bulk parameterization of the snow field in a cloud model, *J. Appl. Meteorol.*, *22*, 1065–1092.

Liu, G. (2008), A database of microwave single-scattering properties for nonspherical ice particles, *Bull. Am. Meteorol. Soc.*, *91*, 1563–1570. doi:10.1175/2008BAMS2486.1.

Masunaga, H., M. Satoh, and Miura, H. (2008), A joint satellite and global CRM analysis of an MJO event: Model diagnosis, *J. Geophys. Res.*, *113*, D17210, doi:10.1029/2008JD009986.

Masunaga, H., T. Matsui, W.-K. Tao, A. Y. Hou, C. D. Kummerow, T. Nakajima, P. Bauer, W. S. Olson, M. Sekiguchi, and T. Y. Nakajima (2010), Satellite Data Simulator Unit: A multisensor, multispectral satellite simulator package, *Bull. Am. Meteorol. Soc.*, *91*, 1625–1632, doi:10.1175/2010BAMS2809.1.

Matsui, T. (2013), Mesoscale model and satellite simulator, in *Mesoscale Meteorological Modeling*, 3rd ed., edited by R. A. Pielke, Academic, San Diego, Calif., in press.

Matsui, T., X. Zeng, W.-K. Tao, H. Masunaga, W. S. Olson, and S. Lang (2009), Evaluation of long-term cloud-resolving model simulations using satellite radiance observations and multifrequency satellite simulators, *J. Atmos. Oceanic Technol.*, *26*, 1261–1274.

Meirold-Mautner, I., C. Prigent, E. Defer, J. R. Pardo, J.-P. Chaboureau, J.-P. Pinty, M. Mech, and S. Crewell (2007), Radiative transfer simulations using mesoscale cloud model outputs: Comparisons with passive microwave and infrared satellite observations for midlatitudes, *J. Atmos. Sci.*, *64*, 1550–1568.

Mitchell, D. L. (1996), Use of mass and area-dimensional power laws for determining precipitation particle terminal velocities, *J. Atmos. Sci.*, *53*, 1710–1723.

Nakajima, T. Y., and T. Nakajima (1995), Wide-area determination of cloud microphysical properties from NOAA AVHRR measurements for FIRE and ASTEX regions, *J. Atmos. Sci.*, *52*, 4043–4059.

Nakajima, T., and M. Tanaka (1986), Matrix formulations for the transfer of solar radiation in a plane-parallel scattering atmosphere, *J. Quant. Spectrosc. Radiat. Transfer*, *35*, 13–21.

Nakajima, T., and M. Tanaka (1988), Algorithms for radiative intensity calculations in moderately thick atmospheres using a truncation approximation, *J. Quant. Spectrosc. Radiat. Transfer*, *40*, 51–69.

Nishizawa, T., H. Okamoto, T. Takemura, N. Sugimoto, I. Matsui, and A. Shimizu (2008), Aerosol retrieval from two-wavelength backscatter and one-wavelength polarization lidar measurement taken during the MR01K02 cruise of the R/V *Mirai* and evaluation of a global aerosol transport model, *J. Geophys. Res.*, *113*, D21201, doi:10.1029/2007JD009640.

Okamoto, H. (2002), Information content of the 95-GHz cloud radar signals: Theoretical assessment of nonsphericity and error evaluation of the discrete dipole approximation, *J. Geophys. Res.*, *107*(D22), 4628, doi:10.1029/2001JD001386.

Okamoto, H., S. Iwasaki, M. Yasui, H. Horie, H. Kuroiwa, and H. Kumagai (2003), An algorithm for retrieval of cloud microphysics using 95-GHz cloud radar and lidar, *J. Geophys. Res.*, *108*(D7), 4226, doi:10.1029/2001JD001225.

Okamoto, H., et al. (2007), Vertical cloud structure observed from shipborne radar and lidar: Mid-latitude case study during the MR01/K02 cruise of the R/V *Mirai*, *J. Geophys. Res.*, *112*, D08216, doi:10.1029/2006JD007628.

Okamoto, H., T. Nishizawa, T. Takemura, K. Sato, H. Kumagai, Y. Ohno, N. Sugimoto, A. Shimizu, I. Matsui, and T. Nakajima (2008), Vertical cloud properties in the tropical western Pacific Ocean: Validation of the CCSR/NIES/FRCGC GCM by shipborne radar and lidar, *J. Geophys. Res.*, *113*, D24213, doi:10.1029/2008JD009812.

Okamoto, H., K. Sato, and Y. Hagihara (2010), Global analysis of ice microphysics from CloudSat and CALIPSO: Incorporation of specular reflection in lidar signals, *J. Geophys. Res.*, *115*, D22209, doi:10.1029/2009JD013383.

Reynolds, R. W., and T. M. Smith (1994), Improved global sea-surface temperature analyses using optimum interpolation, *J. Clim.*, *7*, 929–948.

Rossow, W. B., and Y. Zhang (2010), Evaluation of a statistical model of cloud vertical structure using combined CloudSat and CALIPSO cloud layer profiles, *J. Clim.*, *23*, 6641–6653.

Rutledge, S. A., and P. V. Hobbs (1983), The mesoscale and microscale structure and organization of clouds and precipitation in midlatitude cyclone VIII: A model for the seeder-feeder process in warm frontal rainbands, *J. Atmos. Sci.*, *40*, 1185–1206.

Sato, K., and H. Okamoto (2006), Characterization of *Ze* and LDR of nonspherical and inhomogeneous ice particles for 95-GHz cloud radar: Its implication to microphysical retrievals, *J. Geophys. Res.*, *111*, D22213, doi:10.1029/2005JD006959.

Sato, Y., K. Suzuki, T. Iguchi, I.-J. Choi, H. Kadowaki, and T. Nakajima (2012), Characteristics of correlation statistics between droplet radius and optical thickness of warm clouds simulated by a three-dimensional regional-scale spectral bin microphysics cloud model, *J. Atmos. Sci.*, *69*, 484–503.

Satoh, M., T. Matsuno, H. Tomita, H. Miura, T. Nasuno, and S. Iga (2008), Nonhydrostatic icosahedaral atmospheric model (NICAM) for global cloud resolving simulations, *J. Comput. Phys.*, *227*, 3486–3514, doi:10.1016/j.jcp2007.02.006.

Satoh, M., T. Inoue, and H. Miura (2010), Evaluations of cloud properties of global and local cloud system resolving models using CALIPSO and CloudSat simulators, *J. Geophys. Res.*, *115*, D00H14, doi:10.1029/2009JD012247.

Sekiguchi, M., and T. Nakajima (2008), A k-distribution-based radiation code and its computational optimization for an atmospheric general circulation model, *J. Quant. Spectrosc. Radiat. Transfer*, *109*, 2779–2793.

Shi, J. J., W.-K. Tao, T. Matsui, A. Hou, S. Lang, C. Peters-Lidard, G. Jackson, R. Cifelli, S. Rutledge, and W. Petersen (2010), Microphysical properties of the January 20–22 2007 snow events over Canada: Comparison with in-situ and satellite observations, *J. Appl. Meteorol. Climatol.*, *49*(11), 2246–2266.

Suzuki, K., G. L. Stephens, S. C. van den Heever, and T. Y. Nakajima (2011), Diagnosis of the warm rain process in cloud-resolving models using joint CloudSat and MODIS observations, *J. Atmos. Sci.*, *68*, 2655–2670.

Tomita, H. (2008), New microphysics with five and six categories with diagnostic generation of cloud ice, *J. Meteorol. Soc. Jpn.*, *86A*, 121–142.

Vaughan, M. A., D. M. Winker, and K. A. Powell (2005), CALIOP algorithm theoretical basis document, part 2, feature detection and layer properties algorithms, *Rep. PCSCI202.02*, NASA Langley Res. Cent., Hampton, Va.

Waliser, D. E., et al. (2012), The "year" of tropical convection (May 2008 to April 2010), climate variability and weather highlights, *Bull. Am. Meteorol. Soc.*, *93*, 1189–1218, doi:10.1175/2011BAMS3095.1.

Wiedner, M., C. Prigent, J. R. Pardo, O. Nuissier, J.-P. Chaboureau, J.-P. Pinty, and P. Mascart (2004), Modeling of passive microwave responses in convective situations using output from mesoscale models: Comparison with TRMM/TMI satellite observations, *J. Geophys. Res.*, *109*, D06214, doi:10.1029/2003JD004280.

Yoshida, R., H. Okamoto, Y. Hagihara, and H. Ishimoto (2010), Global analysis of cloud phase and ice crystal orientation from cloud-aerosol lidar and infrared pathfinder satellite observation (CALIPSO) data using attenuated backscattering and depolarization ratio, *J. Geophys. Res.*, *115*, D00H32, doi:10.1029/2009JD012334.

Yuter, S. E., and R. A. Houze Jr. (1995), Three-dimensional kinematic and microphysical evolution of Florida cumulonimbus. Part II: Frequency distributions of vertical velocity, reflectivity, and differential reflectivity, *Mon. Weather Rev.*, *123*, 1941–1963.

Zeng, X., W.-K. Tao, S. Powell, R. Houze Jr., P. Ciesielski, N. Guy, H. Pierce, and T. Matsui (2013), A comparison of the water budgets between clouds from AMMA and TWP-ICE, *J. Atmos. Sci.*, *70*, 487–503.

Zhang, Y., S. A. Klein, J. Boyle, and G. G. Mace (2010), Evaluation of tropical cloud and precipitation statistics of Community Atmosphere Model version 3 using CloudSat and CALIPSO data, *J. Geophys. Res.*, *115*, D12205, doi:10.1029/2009JD012006.